Volume 1
Number 3
May 2017
Pages 399-666
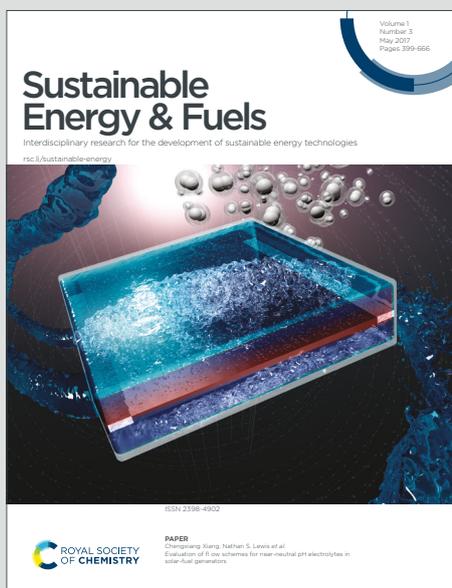
Sustainable
Energy & Fuels

Interdisciplinary research for the development of sustainable energy technologies

rsc.li/sustainable-energy

ISSN 2398-4902

ROYAL SOCIETY OF CHEMISTRY

PAPER
Chengxiang Xiang, Nathan S. Lewis et al.
Evaluation of flow schemes for near-neutral pH electrolytes in solar-fuel generators

This is an Accepted Manuscript, which has been through the Royal Society of Chemistry peer review process and has been accepted for publication.

Accepted Manuscripts are published online shortly after acceptance, before technical editing, formatting and proof reading. Using this free service, authors can make their results available to the community, in citable form, before we publish the edited article. We will replace this Accepted Manuscript with the edited and formatted Advance Article as soon as it is available.

You can find more information about Accepted Manuscripts in the Information for Authors.

Please note that technical editing may introduce minor changes to the text and/or graphics, which may alter content. The journal's standard Terms & Conditions and the Ethical guidelines still apply. In no event shall the Royal Society of Chemistry be held responsible for any errors or omissions in this Accepted Manuscript or any consequences arising from the use of any information it contains.

ROYAL SOCIETY OF CHEMISTRY

rsc.li/sustainable-energy

ARTICLE

Translating Local Binding Energy to a Device Effective one

Dan Liraz,[a] Pei Cheng,[b] Yang Yang[b] and Nir Tessler[a†]

One of the puzzles in the field of organic photovoltaic cells (OPVs) is the high exciton dissociation (charge generation) efficiency even though simple coulomb based arguments would predict binding energy of 150-500 meV that would suppress such dissociation. Not knowing which mechanism drives such high dissociation efficiency does not allow to draw clear design rules. The common approach answering this puzzle is that the binding energy must be lower due to delocalization, disorder or entropy considerations. However, using these theories to quantitatively reproduce the dissociation is challenging. Here, considering entropy and disorder, a new approach is being suggested using the exciton dissociation efficiency as the parameter to weigh the effect of the energetic disorder. The effective entropy-disorder (EED) model predicts the device-equivalent charge generation efficiency, and provides a consistent new definition for the effective binding energy (E_{beff}). For the first time, it is possible to directly compare a model with experimental results of non-fullerene acceptor organic solar cell. Such comparison reveals that high dissociation efficiency does not require E_{beff} lower than 100 meV and that high dissociation efficiency is driven by a combined effect of the energy landscape and a mobility which is significantly higher than the steady state one.

Introduction

Bulk heterojunction (BHJ) organic solar cells have been gaining momentum with the introduction of nonfullerene acceptors (NFAs).[1-4] The power conversion efficiency (PCE) has been rising steadily with current champion devices being around 16% [5, 6] of single junction devices and more than 17% of tandem structures,[7] where a new evaluation of the efficiency limit still place it at about 20% for single junction.[8] PCE losses may occur due to open circuit voltage (V_{oc}) loss or short circuit current (J_{sc}) loss where V_{oc} loss through radiative recombination is inevitable. The Holy Grail is to avoid any other losses such that the internal quantum efficiency (IQE – extracted photoelectrons to absorbed photons) would be almost 100%, as is indeed the case with some of the state of the art devices.

Current losses may appear in several steps on the way of converting photon flux to an electric current. Absorption creates excitons that may decay while diffusing towards the donor/acceptor (D/A) interface. After a charge is transferred to the other side of the interface, the charge transfer state exciton (CT exciton state) may decay before dissociating to polaron pair. Lastly, polarons may recombine before being collected by the respective contacts. The IQE is a multiplication of exciton to CT, CT dissociation, polarons transport and collection efficiencies.[9] For highly efficient devices, each of these steps should be close

to 100% efficient. Thus, one of the key factors in achieving a high-efficiency cell is the exciton dissociation (i.e. charge generation) efficiency, which has been pointed out as being too high for NFA devices if the binding energy was calculated using Coulomb attraction between two point charges.[10] Regarding the CT exciton state, it has been confirmed by several methods that a CT exciton state is a nearest-neighbor pair.[11, 12] This emphasizes the difficulty of dissociating the CT state without significant losses associated with geminate recombination. There have been several suggestions of mechanisms lowering the effective binding energy of the excitons as delocalization and dipole effect,[13-15] disorder,[15-19] and entropy.[19-22] Examining the literature, we find that it is common to describe the binding energy as the internal energy difference between the bound state and the state where two separate charges reside on two molecules distanced enough to neglect any interaction between them.[23] This definition is most natural for one CT exciton in a 1D system.[20] It has also been shown that the coulomb binding or internal energy difference is unchanged when considering 3D systems.[15] However, for 3D systems there are many more than one path the CT state may dissociate through and one must take thermodynamics considerations into account,[20] assuming the energy required to dissociate the excitons to free charges is the quantity of interest.

Moreover, the relation between the observable used to deduce the effective (macro) binding energy of a cell and the (micro-local) binding energy of an isolated pair is hardly discussed. Namely, it is difficult to use previous relevant works[19] to quantitatively predict/analyze the cell's charge generation efficiency. We find that this is especially important in the presence of disorder and we look into the effect of entropy and disorder on the free-charge generation efficiency with the effective binding energy being determined by it (and not vice

[a.] Microelectronic & Nanoelectronic Centers, Electrical Engineering Department, Technion Israel Institute of Technology, Haifa (Israel). Email: nir@technion.ac.il
[b.] Department of Materials Science and Engineering, University of California, Los Angeles, CA, USA.

versa). To explain the transformation from an ensemble of pairs to effective dissociation efficiency and to a single effective binding energy, we present histograms of the binding energies and of the dissociation distance. We also employ it to justify the use of a bi-layer model to predict the performance of BHJ.

Having established the effective entropy-disorder (EED) model, that relates to measured efficiency, we use the model system of polymer:NFA device, PTB7-Th:ITIC BHJ to show a correlation between the theoretical predictions and the temperature dependent properties of the cell. By self-consistently analyzing the device data and the model's results we confirm that entropy and disorder indeed play a major role in the exciton dissociation. Lastly, we discuss several approaches of defining binding energy for a macroscopic system and reveal the fact that for realistic, disordered devices, the microscopic, well-defined, binding energy does not correlate directly with the macroscopic effective binding energy.

To make our work better accessible we include below, as part of the introduction, a brief review of the concepts that are directly used here.

Why it is correct to use thermodynamics and why we must?

In this work, first we discuss defining the local binding energy using thermodynamics and later we translate it to a macro, device-equivalent, binding energy. Defining CT exciton binding energy by the internal energy difference between bound state and nonbound state does not capture entirely the physics of the system. Specifically, it does not describe the average thermal energy required to dissociate excitons. In a real case of operating device, excitons are being formed continuously in the volume of the device, diffuse to the interface and create CT states. Focusing on one nearest neighbor pair of molecular sites along the interface; CT state would be created in this position, dissociate or recombine and later a new CT state would be created there and so forth. Although all these CT states start dissociating from the same position and there is only one way to describe them, in 3D system, the resulting free polarons have many optional positions to dissociate to, so there are plenty of ways to describe this situation. This reflects in a lower probability for the CT state to stay at its initial position or a higher probability for dissociation. It is common to consider only the coulomb potential (i.e. the internal energy difference) which acts to keep the electron-hole of the CT state stick together. However, to understand the local CT state dissociation, we must take into account both effects through the use of thermodynamics. In our discussion we neglect possible contributions from lattice (molecular) relaxations.[23]

Some of the thermodynamic results we shall use require thermal equilibrium. An operational OPV device is not at equilibrium as it is excited by a photon flux. However, the system under consideration is the CT state itself. Since we are not interested here in the possible contribution from hot-CT dissociation we may proceed with the assumption that the CT is fully relaxed in the molecular sites before it dissociates. We refer to the situation as quasi-equilibrium state, because while the whole system may be out of equilibrium, the CT state is locally relaxed.

Free energy, entropy, partition function, and disorder

It is well known that to reach (quasi) equilibrium a system would evolve so as to minimize its potential energy. However, in realistic systems, there are constraints, the system may be forced to keep constant volume (isochoric) or pressure (isobaric) or temperature (isothermal). In this situation, the minimization is of a thermodynamic potential. For an isothermal and isobaric process, Gibbs free energy is the suitable thermodynamic potential, defined as:

$$G = U - TS + PV \tag{1}$$

Where U is internal energy, S is the entropy, P is pressure and V is volume.

For isothermal processes, the Helmholtz free energy F is minimized at equilibrium.

$$F = U - TS \tag{2}$$

For systems having constant pressure and volume, as in our case, there is no difference between minimizing F or G. In the following the Gibbs free energy is the one of interest but for energy minimization purpose, F is used.

The entropy is a macroscopic property that depends on the number of configurations or microstates available to the system. The entropy is defined by:

$$S(X = \alpha) = -k_b \sum_i^{\Omega(X=\alpha)} p_i \ln(p_i) \tag{3}$$

Here, X is a macroscopic property, $\Omega(X=\alpha)$ is the number of microscopic configurations that their X equals α, i is the index of a microstate (configuration) with X=α, and p_i is the probability of the microstate i to be occupied given the macrostate is α. In the context of exciton dissociation or charge pairs, X may be the distance between the charges in the pair where X=α includes all pairs' configurations where the charges are separated by distance α (r=α) and p_i is the probability for a specific pair configuration, with separation r=α, to be found (occupied).

To find p_i we recall that the microstate i is associated with internal energy ε_i. For a system like the one we are interested in (canonical ensemble) the probability of a state carrying internal energy ε_i follows the Maxwell-Boltzmann distribution:

$$p_i = \frac{\exp\left(-\dfrac{\varepsilon_i}{k_b T}\right)}{Z} \tag{4}$$

$$Z = \sum_i^{\Omega(X=\alpha)} \exp\left(-\frac{\varepsilon_i}{k_b T}\right)$$

Where is called the partition function and serves as a normalization factor of the probability, which makes sure all probabilities sum to one. In case all microstates (pairs' configurations of distance r=α) are characterized by the same energy ($\varepsilon_i=\varepsilon$), equation (3) can be presented as $S(X=\alpha) = k_b \ln[\Omega(X=\alpha)]$. However, we will use the more general form of equation (3). A useful relation describing the Helmholtz free energy is:

$$F = U - TS = -k_b T \ln(Z) \tag{5}$$

Disordered Heterojunction To calculate the contribution of the microstates (charge pair configurations) to the entropy (equation (3) and (4)) we need to assign energy to each configuration. For an organic heterojunction, the most natural choice would be the difference between the electron energy at the acceptor site and the hole energy at the donor site. This would be the difference between acceptor's LUMO (lowest unoccupied molecular orbital) and donor's HOMO (highest occupied molecular orbital) plus the coulomb interaction. For ordered materials the LUMO-HOMO difference would be constant between all microstates and for any r. For disordered materials there would be fluctuations of these values. It is common to describe such electronic disorder as a Gaussian distribution characterized by a mean value (E_0) and a standard deviation (σ). In this case, the energy difference between the electron on acceptor site and hole on donor site would also have a gaussian distribution. This difference, between the charge pair energies, will have a fluctuation (δ) having a standard deviation of $\sigma_{cp} = \sqrt{\sigma_a^2 + \sigma_d^2}$, where σ_a and σ_d are the standard deviations of the acceptor and donor levels, respectively. With 'i' being the index used for counting the possible pair configurations (microstates), we may write the energy as the sum of coulomb potential and the energy introduced by the disorder:[19]

$$\varepsilon_i(r) = -\frac{q}{4\pi\varepsilon\varepsilon_0 r} + \delta_i \tag{6}$$

Where we disregarded the constant E_0 which is just an energy offset. For the ordered case $\delta=0$ and all microstates, of constant r, have the same energy, leading to $p_{i,ordered}(r) = 1/\Omega(r)$ and $S_{ordered} = k_b \ln(\Omega(r))$.

For the disordered case, the partition function is:

$$Z(r) = \sum_i^{\Omega(r)} \exp\left(-\frac{-\frac{q}{4\pi\varepsilon\varepsilon_0 r} + \delta_i}{k_b T}\right) \tag{7}$$

Which defines the Helmholtz free energy, F, according to equation (5).

It is worth mentioning that using equation (4) and (7) and the entropy definition in equation (3) one can derive:
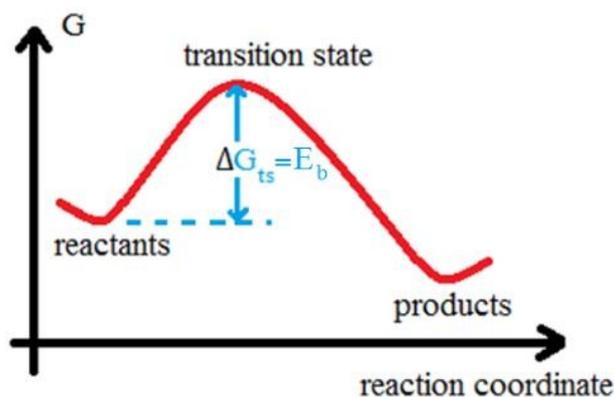

Figure 1. Elementary reaction profile

$$S(r) = \frac{1}{T} \frac{\sum_i^{\Omega(r)} \delta_i \exp\left(-\frac{\delta_i}{k_b T}\right)}{\sum_i^{\Omega(r)} \exp\left(-\frac{\delta_i}{k_b T}\right)} + k_b \ln\left\{\sum_i^{\Omega(r)}\left[\exp\left(-\frac{\delta_i}{k_b T}\right)\right]\right\} \tag{8}$$

Equation (8) shows that, for the disordered case, the entropy is temperature dependent. This is an important result as it implies, that for a disordered system, the entropy would have a larger impact on the temperature dependence of the apparent dissociation efficiency or effective binding energy.

Exciton dissociation as a Process rate – Onsager Braun and Eyring-Polanyi equations

Lars Onsager analyzed exciton dissociation using a diffusion, Brownian motion differential equation with the effect of Coulomb interaction and external field. [24, 25] In his model, the CT pair has one opportunity to dissociate, failure leads to decay. Braun used Onsager work [10] but in his treatment, the CT has a finite lifetime. This gives the CT ability to make several dissociation-attempts before it decays. To deduce relevant parameters, the Onsager-Braun model assumes a detailed balance between the CTs dissociation and the Langevin process of bimolecular recombination.

The basic idea behind Onsager-Braun model is that CT dissociation is an energy activated process, as suggested by Arrhenius equation. However, Arrhenius equation is empirical [26] and it may serve to solve a case when the entropy and enthalpy are constant during the reaction. The general term that one should use is the Eyring-Polanyi equation which is part of the transition state theory (Figure 1). The transition state theory assumes equilibrium between reactants and the transition state such that the overall forward reaction rate is governed by ΔG_{ts} instead of internal energy difference dictated by Arrhenius.

As Figure 1 shows, the local binding energy is the added free Gibbs energy required to reach the peak of the potential. Integrating Eyring-Polanyi equation, where ΔG_{ts} serves as binding energy, with Onsager-Braun model which predicts dissociation efficiency as a result of two competitive reactions, CT dissociation, and CT decay, the dissociation efficiency can be expressed as:

$$\eta_{dissocialion} = \frac{k_{ed}}{k_{ed}+k_{decay}} = \frac{\kappa_{cd}\cdot\exp\left(-\frac{\Delta G_{ts}}{k_b T}\right)}{\kappa_{cd}\cdot\exp\left(-\frac{\Delta G_{ts}}{k_b T}\right)+k_{decay}} = \frac{k_{cd}\cdot\exp\left(-\frac{E_b}{k_b T}\right)}{k_{cd}\cdot\exp\left(-\frac{E_b}{k_b T}\right)+\frac{1}{\tau_{CT}}} \tag{9}$$

Where k_{ed} is the dissociation rate, k_{decay} is the CT state decay rate, κ_{cd} is proportional to squared overlap integral of initial and final states, E_b is the CT state binding energy, k_b is Boltzmann constant, T is temperature and τ_{CT} is CT lifetime.

Applying the thermodynamic concepts to organic heterojunction
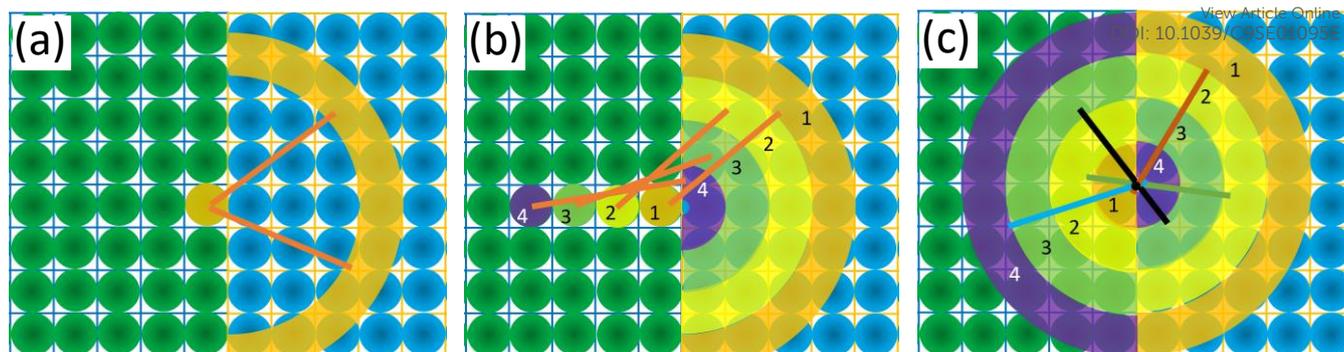
The charge pairs as microstates

Figure 2. Illustration of the counting of pair configurations available for charge pairs with separation distance r. Consider that each rectangular is one site as in a molecule or a conjugated element where the particle is delocalized. (a) The left side of the charge-pair is static, and the counterpart charge can be hosted on any of the sites in the yellow hemisphere. (b) The left side of the charge-pair is mobile and hence can be in any site along a line perpendicular to the interface. Site i (on the left) forms an r-separated pair configuration with all sites within hemisphere i (on the right). Ω would be a summation over all i contributions. (c) A similar counting as in b but, to avoid the assumption of symmetric junction, the counting is done by fixing the point at which the line that connects the pair crosses the interface. Again, each site located in the right hemisphere i forms an r-separated pair configuration with site/s in the left hemisphere i. The r-long lines demonstrate some of the possible r-separated pair configurations. Here too, Ω is a summation over all i contributions.

The more paths/options the exciton can dissociate through, the higher would be the probability for dissociation (dissociation efficiency). When the exciton transforms from nearest neighbor charges (exciton) to charges distanced from each other (charge pair) we say that it transferred from the initial microstate to a target microstate. In the context of CT exciton dissociation, it is common to group the microstates into a macrostate according to the distance (r) between the hole on the donor and the electron on the acceptor.[19, 20] For example, Figure 2a illustrates a heterojunction where one charge is static near the interface and all the microstates (charge pair configurations), that have charge separation 'r', are the combination of the static site and the hemisphere on the right-hand side of the junction. In such a case, Ω(r) (see equation (3)) is the number of sites on the right-hand side of the junction which touch the sphere (see Figure 2a). This calculation results in $\Omega(r) \alpha r^2$ [20] as would be expected from an area of a spherical sector.

Ω(r) significance lies in finding ΔG_{ts} by using equation (5), (6), and (7) to calculate the elementary reaction profile (Figure 1) where the charge separation r is taken as the reaction coordinate. To account for both charges being able to depart from the interface, an iterative method was suggested[19] where the sphere center is allowed to move along a line perpendicular to the donor-acceptor interface (see Figure 2b). The total count of available configurations, Ω(r), is now a result of summation over all contributions of centers along this axis. This method leads to a result, which is close to the number of states enclosed in a hemisphere, in this case $\Omega(r) \alpha r^3$ (Figure 2b). [19]

Having the center of the sphere within one side of the junction carries a hidden assumption that the junction is symmetric in terms of packing and mobility. We propose a third approach of counting configurations. First, we choose a static point 'j' on the interface. This point can be considered as the place where the CT was originally formed as a nearest-neighbor pair. We count all pairs that are connected by r-long line crossing the interface at point 'j' (see Figure 2c). Later we show that the CT dissociate close to the interface, thus it is logical to assume that point 'j' is almost static during the dissociation process. The advantage of

this counting method is that it allows the use of two different packings on either side of the junction.

In the supplementary materials, we describe in detail our method of calculating Ω(r). For all examined geometries we got the phenomenological behavior of $\Omega(r)=a \cdot r^3$. However, 'a' is geometry (morphology) dependent and may vary by up to a factor of 3 thus affecting the quantitative results of the calculation.

There is also another subtle point that is especially important in the context of disorder. Unlike previous works,[19, 20] which used Ω(r) only as a upper bound of summation, for a given environment we first generate a 3D lattice of disordered heterojunction and perform all calculation with the aid of this lattice (similarly to the approach taken by Monte-Carlo simulations). This accounts for the built-in correlation associated with the fact that each site may be part of several r-distinguished pair-configurations. In the following we use a 3D geometry which is cubic and with lattice constant of 1 nm.

From the energy landscape of a single charge pair to the dissociation efficiency of a complete device

Knowing to derive the local binding energy using thermodynamics, we are ready to translate it to device equivalent binding energy. In the following, we consider that for a disordered film there is a built-in spatial distribution (dispersion) of the density of states.[27, 28] Namely, the local environment surrounding a given CT exciton depends on the specific position of this CT within the macroscopic device. As a result, at different positions within the device the binding energy, as well as the dissociation efficiency, could be different. To demonstrate this, we will examine the free energy change experienced by CT excitons generated in different environments. As mentioned above, each environment is created by generating a 3D lattice of sites' energies. Using equation (5), the Helmholtz free energy (F) as a function of charge separation (r) is:

$$F_j(r) = -k_b T \ln\left(\sum_i^{\Omega(r)} \exp\left(-\frac{-\frac{q}{4\pi\varepsilon\varepsilon_0 r} + \delta_j(i)}{k_b T} \right) \right) \quad (10)$$

Where we have added the subscript j to denote a specific environment (or a given draw of state energy distribution) along the donor/acceptor interface. In Figure 2c 'j' would refer to the crossing point that is used for evaluating $\Omega(r)$. The change in free energy, $\Delta F_j(r)$ or $\Delta G_j(r)$ which are the same in our system, is calculated relative to the initially generated CT exciton (at minimum r, which is nearest-neighbors distance). As was discussed in the context of Figure 1, the maximum of this change in free energy is the local/microscopic binding energy of the CT exciton in environment j.

Figure 3 demonstrates the extraction procedure of three binding energies from three $\Delta G_j(r)$ graphs. $\Delta G_{ts,j}$ ($\Delta G_j(r)$ maximum value) is the CT local binding energy $E_{b,j}$, and the r position of this maximum is the maximum separation length before the CT dissociates spontaneously (we term this "dissociation distance"). $\Delta G_j(r)$ graph was produced by subtracting the initial Helmholtz free energy $F_j(r=1)$ from r separated CT excitons Helmholtz free energy $F_j(r)$ (inset to Figure 3).

As for different environments (draw of states energies) both the local binding energy and local dissociation distance vary, one needs to examine a large number of environments to reproduce the full device. The challenge would be in finding the most suitable method to represent the properties of the complete device. To illustrate the dispersion in the local properties, Figure
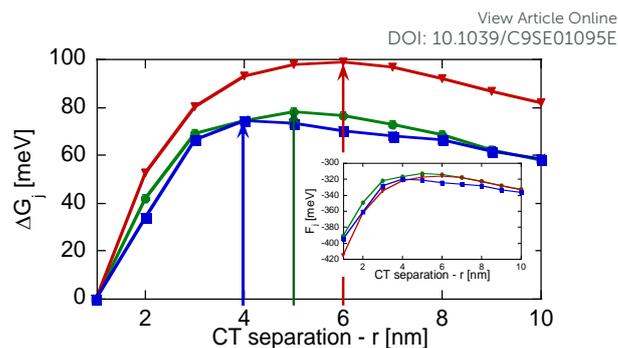

Figure 3. ΔG_j as a function of CT's charge separation for three different CTs environments, all for junction disorder standard deviation (σ_{cp}) of 50 meV at 300 °K. The edge of the arrows represent the binding energy of each CT (in j environment) and their crossing with the x-axis denotes the maximum separation lengths before the CTs dissociate. Inset shows the F_j of the three environments.

4 shows the statistical analysis of such environments in terms of binding energy distribution and dissociation distance distribution for several junction energy disorder parameter σ_{cp} (CP stands for charge pair). We apply the EED model on a cubic geometry with lattice constant of 1 nm and assume $\varepsilon=3.3$. Figure 4a and Figure 4b show the normalized distribution of the binding energies assuming T=200 °K and T=300 °K, respectively. Figure 4c and Figure 4d show the normalized distribution of the dissociation distance assuming T=200 °K and T=300 °K, respectively. The symbols denote the results of the analysis and the full lines are Gaussian fits to the data points.

Figure 4 shows that as the junction disorder parameter (σ_{cp}) increases, the distributions of both the binding energy and dissociation distance shift towards zero and broaden.
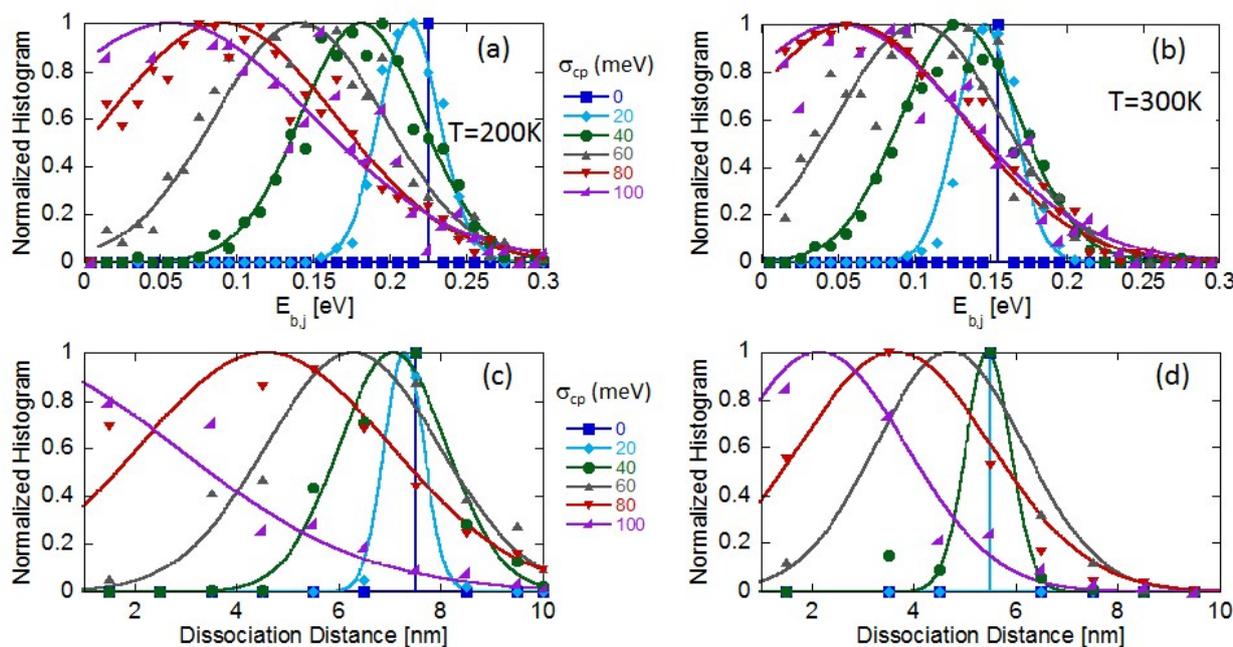

Figure 4. (a) and (b) are the normalized distributions of the local binding energy ($E_{b,j}$) at 200 °K and at 300 °K, respectively. (c) and (d) are the normalized distributions of the dissociation distance at 200 °K and at 300 °K, respectively. Symbols are the simulation results and solid lines are Gaussian fits. Blue, cyan, green, grey, red, and magenta lines are simulation results for junction disorder standard deviation (σ_{cp}) of 0 meV, 20 meV, 40 meV, 60 meV, 80 meV, and 100 meV, respectively.

Comparing the results for the two temperatures we note that both the binding energy and dissociation distance tend to be larger at lower temperature and that the differences between the results for the two temperatures almost disappear for the high σ_{cp} values. The most probable dissociation distance is below 6 nm (see also ref 12) and at room temperature the entire distribution of dissociation distance (Figure 4d) lies below 10 nm. The latter suggests that although we are treating a bi-layer architecture the results would be applicable to BHJ devices, most of which have above 10 nm fine structure. To place the values in a broader context we note that in the absence of the effects considered here (entropy and disorder) the dissociation distance is taken as the point where the coulomb binding energy equals the thermal energy $q^2/4\pi\varepsilon\varepsilon_o r_{max} = k_bT$. For a typical organic device ($\varepsilon \approx 3.3$) at room temperature, the dissociation distance is about 17 nm.

The fact that disorder reduces the microscopic binding energy, as well as the dissociation distance, is well known. [12, 15, 19, 21, 29] However, translating the spatial variation across the sample to device measured properties, as effective dissociation efficiency or effective binding energy, is not obvious. Previous works averaged the ΔG curves (as those in Figure 3) to obtain average potential from which a macroscopic binding energy was derived. Such approach shows that, with the introduction of disorder, [19] the resulting binding energy reduces towards zero (see Figure 8Sm in the supplementary materials). Next step was to conclude, qualitatively, high dissociation efficiency from the reduced effective binding energy. However, this approach fails to give quantitative reproduction of measured curves. In addition, it is not clear how to account for exciton lifetime and the charge hopping rate (mobility) or how to use the results to evaluate the effective exciton dissociation (charge generation) efficiency.

We take a different approach and suggest doing the opposite. Meaning to use the local exciton dissociation efficiency to derive the effective (device equivalent) exciton dissociation efficiency and deduce the effective binding energy from it. While this may seem a minor difference, it results in a very different effective medium which is now similar to the approach taken by Monte-Carlo simulations (detailed quantitative comparison of the different approaches appears in supplementary materials). [30-33] Our approached is motivated by

the understanding that when one is interested in a device effective quantity one should average over the property that is being measured and by the most common property used being the current. The light induced current is a linear summation of contributions of dissociated CT excitons. The probability for each CT to dissociate and contribute to the current is its local dissociation efficiency. Thus, arithmetic mean over local dissociation efficiency is proportional to the light induced current. Consequently, we define the effective dissociation efficiency as averaged local dissociation efficiency. The implementation of our new approach is straight forward once the local binding energies ($E_{b,j}$) have been found. Using equation (9) we may write the device related effective dissociation efficiency as the sum-average of the local (microscopic) dissociation efficiency:

$$\eta_{cd,eff} = \langle \eta_{cd,j} \rangle_j = \left\langle \frac{\exp\left(-\dfrac{E_{b,j}}{k_bT}\right)}{\exp\left(-\dfrac{E_{b,j}}{k_bT}\right) + \dfrac{k_{decay}}{\kappa_{cd}}} \right\rangle_j \qquad (11)$$

Once the device equivalent dissociation efficiency ($\eta_{cd,eff}$) is obtained, the most reasonable definition for the effective binding energy ($E_{b,eff}$) is by using $\eta_{cd,eff}$ and equation (9):

$$E_{b,eff} = -k_bT\left[\ln\left(\frac{\eta_{cd,eff}}{(1-\eta_{cd,eff})}\right) + \ln\left(\frac{k_{decay}}{\kappa_{cd}}\right)\right] \qquad (12)$$

The above equations indicate that $\eta_{cd,eff}$ and $E_{b,eff}$ are temperature, disorder, and k_{decay}/κ_{cd} (or $\kappa_{cd}\cdot\tau_{CT}$) dependent. To illustrate the above we apply equation (11) to simulated samples having different junction disorder parameter (σ_{cp}) and for a range of temperatures. For this calculation we used κ_{cd} of $3.65\cdot10^9$ s^{-1} which is a result of classic estimation using Onsager-Braun work [10] and assuming the active layer mobility is 10^{-4} cm^{2}s^{-1}V^{-1}. [34, 35] We note that 10^{-4} cm^{2}s^{-1}V^{-1} is the steady state mobility and that there are arguments for using a higher "non-relaxed" mobility value. We return to this point in the experimental analysis section. For the CT lifetime (τ_{CT}) we use 10 ns as it is in the reasonable range for organic devices. [36] The resulting dissociation efficiency ($\eta_{cd,eff}$) as a function of inverse temperature (1000/T) is shown in Figure 5a. The top curve (dashed grey) is for σ_{cp}=110 meV and the bottom one (dashed black) is for the ordered case σ_{cp}=0 meV. All the other curves have σ_{cp} in between, as depicted by the legend. As would be
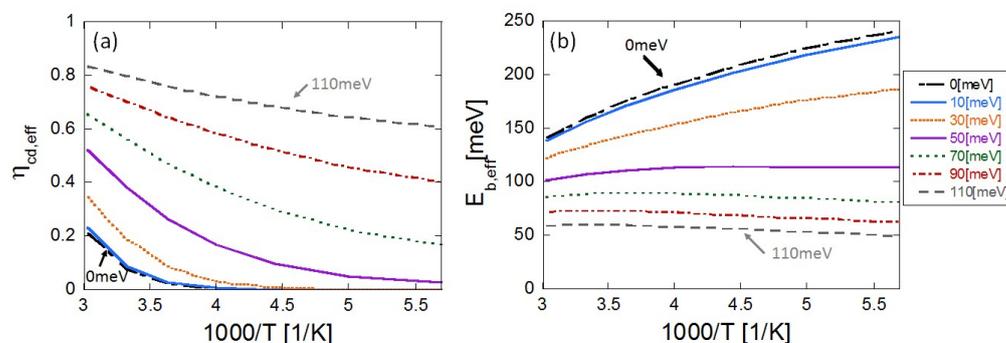

Figure 5. a) Simulated device equivalent CT exciton dissociation-efficiency as a function of inverse temperature (1000/T) and for a range of junction disorder parameters (σ_{cp}). b) The deduced effective binding energy, equation (12), as a function of inverse temperature (1000/T) and for a range of junction disorder parameters (σ_{cp}). Note that in a) the higher disorder is the top curve and in b) it is the lowest (see legend).

expected, an increase in the junction disorder parameter (σ_{cp}) results in enhanced dissociation efficiency. The unique features of our approach is that the dissociation is now quantified and it reveals that the temperature dependence (i.e. its functional form) changes significantly as a function of disorder.

Once the device equivalent dissociation efficiency ($\eta_{cd,eff}$) is obtained (Figure 5a), equation (12) can be applied to obtain the resulting effective binding energy ($E_{b,eff}$). Figure 5b shows that at low disorder the effective binding energy goes down with temperature and the slope is -T. In the presence of disorder, the contribution of the entropy changes, becomes temperature dependent, and at high disorder the slope of $E_{b,eff}$ changes its sign. Within the framework of the current paper, an effective binding energy that goes up with temperature is a clear sign of disorder.

As seen in Figure 5b the new effective binding energy definition does not converge to zero and seems more realistic than in previous works.[19] Further discussion about $\eta_{cd,eff}$ and $E_{b,eff}$ dependencies on CT lifetime and mobility appear in the supplementary materials.

Experimental analysis of NFA OPV device

To test the validity of the model suggested above we compare it to measurements performed on non-fullerene acceptor (NFA) device composed of PTB7-th:ITIC (see Figure 6a for the chemical structures). To set the scene we show in Figure 6a the J-V curve of the device under one sun illumination with the left inset presenting the quantum efficiency spectral response under low light intensity. Also shown is the energy level diagram for the two materials separately. Due to the limited accuracy and the difference between the two methods used to derive the energy levels we slightly rounded the reported value.[37, 38] The extracted cell's parameters are open circuit voltage V_{OC}=0.82 V, short circuit current J_{SC}=13 mAcm^{-2}, fill factor FF=60%, and power conversion efficiency PCE=6.5%. The spectral dependence of the external quantum efficiency (EQE – left inset to Figure 6a) predicts that in the ideal case, the open circuit voltage dictated only by radiative recombination is V_{OC_rad}=1.0 V ($\Delta V_{OC,nrad}$ =0.18 V).

To be able to correlate the device performance with the model's predictions we repeated the J-V measurements over a wide range of light intensities and temperatures. Although we are primarily interested in the charge generation (exciton dissociation) process we first look into the recombination process (Figure 6b and Figure 6c). To find the type of recombination process taking place in the PTB7-th:ITIC NFA OPV we present both the dark J-V (Figure 6b) and the open circuit voltage versus light intensity (Figure 6c) for a range of temperatures. Figure 6d shows the extracted ideality factors which are all above 1.4, indicating significant contribution of trap assisted recombination.

The data that is more directly related to the exciton dissociation process is shown in Figure 6e and Figure 6f. Figure 6e and Figure 6f show the Internal quantum efficiency (IQE), measured using white light emitting diode (LED), as a function of light intensity and temperature, respectively. To translate the EQE measured

under white light to IQE, we normalized the values such that at room temperature and at zero bias it will coincide with the peak of the IQE spectrum, measured under the same conditions. The IQE spectrum was derived using the measured EQE spectrum and the reflectance spectrum of the cell (see supplementary Figure 12s). In Figure 6e, the applied bias was 0.5 V and the different curves are for different substrate temperatures. We chose 0.5 V to minimize the internal field and at the same time to ensure the bias is below V_{oc} even at high temperatures (see Figure 6c). The concept of intensity dependent measurement[39-41] is that at low light intensity the recombination losses are minimized and the plateau region is where recombination between light-generated charges is negligible. Thus, this low intensity IQE is most likely to represent the effective dissociation efficiency and may serve us to compare measurement and theory. According to Figure 6e, the intensity of 1mWcm^{-2} is in the low intensity range and hence can be used to examine the charge generation, or exciton dissociation, efficiency.

In principle, the light intensity dependence can be used to identify signatures of trap-filling of the trap-assisted recombination and of the bi-molecular recombination.[39-41] In our case, examining the higher intensity range, one cannot identify any signature of trap-filling for the trap-assisted recombination. Since Figure 6d clearly shows that trap-assisted recombination is rather dominant, we are left to conclude that the traps are already full at low light intensity or rather are already full under dark conditions.[40]

Figure 6f shows the temperature dependence of the IQE measured at 1 mWcm^{-2} and for a range of applied bias. We note that towards room temperature the IQE increase tends to saturate and that as a function of bias it saturates towards -1 V. At room temperature, the relative increase of the IQE between +0.5 V and -1 V is ~30%. This 30% difference could be either due to field dependent charge generation[10] or to recombination with the dark charges[40, 42] that are injected under forward bias. The results discussed above are clearly for the recombination with the dark charges through trap-assisted recombination,[40] and we return to this point in the following sub section.

Comparing with the theoretical predictions

Having collected the information regarding the PTB7-Th:ITIC BHJ OPV device we move to compare with the EED model developed in this paper. When doing so, one has to remember the limited scope of the model and specifically that it does not account for the potential effect of the electric field on the exciton dissociation.[10] Neither does it account for the recombination that may be induced through the injection of dark charges under forward bias.[40]

With the above limitations in mind we chose to fit the curve closest to V_{OC}, i.e. at +0.5V, and rely on the fact that the theory (Figure 5) predicts that not only the absolute value of the efficiency changes with disorder but also that its temperature dependence (functional form) is significantly dependent on the junction disorder (σ_{cp}). Assuming the mobility relevant for the charge dissociation is the steady state one, Figure 5 was already

calculated using parameters suitable for the measured device ($\mu=10^{-4}$ cm^{2}s^{-1}V^{-1}, τ_{CT} =10 ns).[34-36, 43] Figure 7a shows the measured internal quantum efficiency (symbols) overlaid on the calculated dissociation efficiency curves. The best fit is found for a junction disorder of σ_{cp}=90 meV with the discrepancy being mainly at room temperature. Using the same material parameters ($\mu=10^{-4}$ cm^{2}s^{-1}V^{-1}, τ_{CT} =10 ns) we can use equation (12) to deduce the effective binding energy, that corresponds to the measured dissociation efficiency, and the resulting values are shown in Figure 7b. The deduced effective binding energies are indeed with a slope that is indicative of disorder and the

room temperature value corresponding to the measured data is $E_{b,eff}$ = 90 meV.

By overlapping the measured IQE with the predicted effective dissociation efficiency we found that the best fit is with junction disorder ($\sigma_{cp}=\sqrt{\sigma_d^2+\sigma_a^2}$) of about 90 meV (Figure 7a). This disorder magnitude is in accordance with previous works on this materials system. According to ref [34] the disorder of ITIC mixed with PTB7-th is about σ_a = 70 meV and ref [44] shows that PBT7-th has about σ_d = 70 meV when mixed with fullerenes (i.e. $\sigma_{cp} \cong$ 100 meV). The fact that overlapping the model and
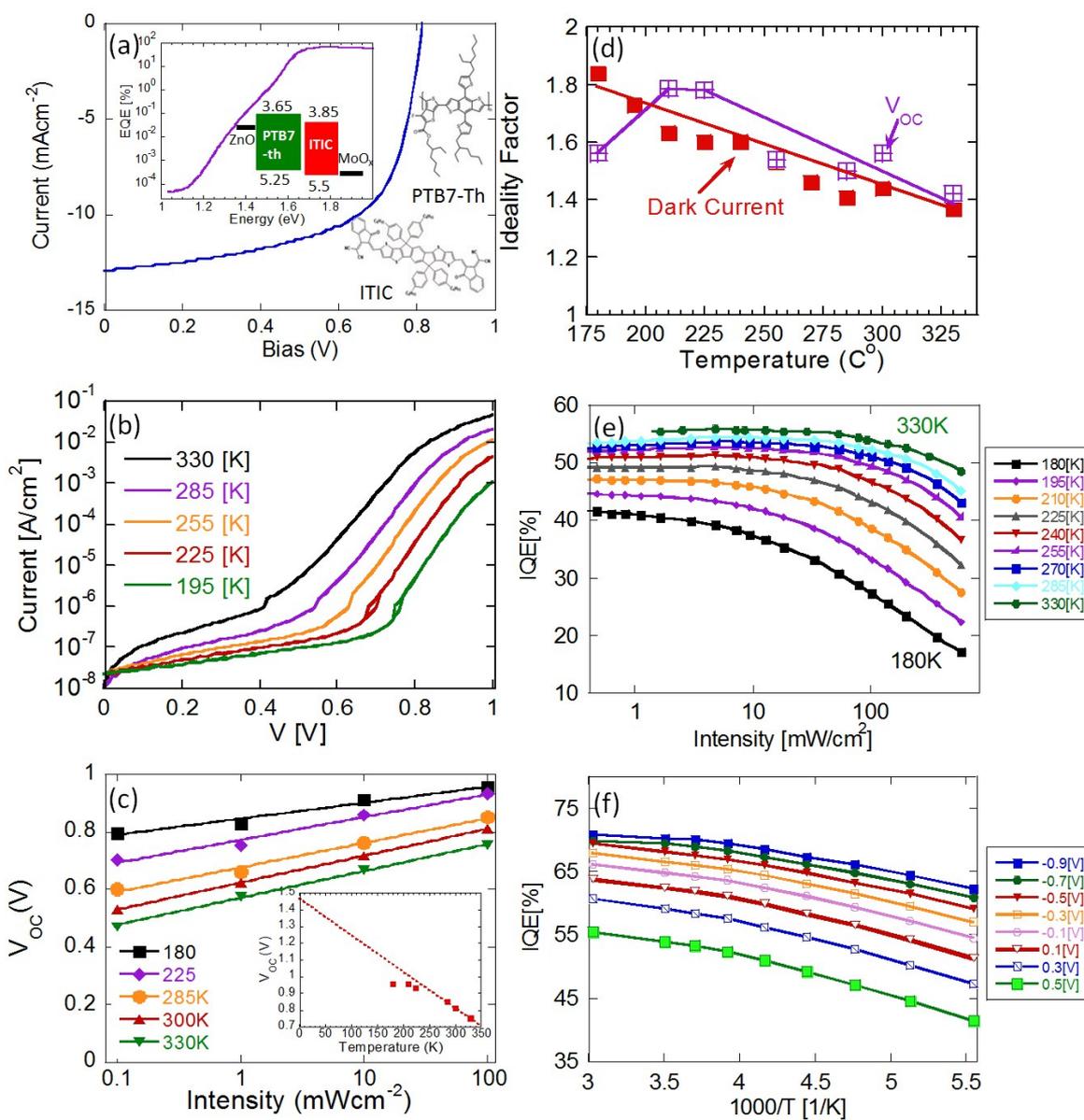

Figure 6 - (a) Current density-Voltage curve under one sun illumination for PTB7-th:ITIC BHJ device. Left inset shows the wavelength dependent external quantum efficiency measured under very low light intensity as well as the energy level diagram of PTB7-th and ITIC. Right inset shows chemical structure of the PTB7-Th donor polymer and of the ITIC acceptor molecule. (b) Measured dark current-voltage curves for a range of temperatures. (c) Measured open circuit voltage (V$_{OC}$) as a function of excitation light intensity, for a range of temperatures. Inset shows the open circuit voltage, at 1 Sun, as a function of temperature. The dashed line is extrapolation to find the effective bandgap (1.47eV) (d) Extracted ideality factor values from the dark current (full red squares) and from the open circuit voltage (purple squares). Lines are only a guides to the eye. (e) Internal quantum efficiency (IQE) as a function of excitation intensity and for a range of temperatures. Applied bias was 0.5 V. (f) IQE as a function of inverse temperature and for a range of applied bias. Excitation intensity was 1 mWcm^{-2}.

experiment yields the film's disorder, suggests that the model captures at least part of the physics.

However, we note that the functional form of the predicted curves does not reproduce the saturation in dissociation efficiency at high temperatures. Moreover, one should keep in mind that our analysis of Figure 6d and Figure 6e indicated that trap assisted recombination contributes an intensity-independent loss. Namely, the actual dissociation efficiency should be higher than the measured low-intensity IQE. Also, in the model we make use of the Onsager-Braun theory, and to derive the value for the escape rate (κ_{cd}) we used the steady state mobility of 10^{-4} cm^{2}s^{-1}V^{-1}. However, the Onsager-Braun theory did not consider the presence of disorder. One could argue that the mobility to be used should thus be the one that would have existed if the material was energetically ordered (i.e a few orders of magnitude higher). A different argument would lead to a similar conclusion. Figure 4d shows that the charges can be considered separated at a distance below 6 nm. By moving only a few nm the charges do not get "trapped" by the low density of low energy sites and their motion is represented by the instantaneous mobility.[45] To check if this could be the source of the discrepancies, we use the disorder of $\sigma_a=\sigma_d=70$ meV and theories on charge transport in disordered media to

deduce that in the ordered case the mobility would be 1-2 orders of magnitude higher. [46, 47] We take the limit of 2 orders and repeat the procedure, of matching model to experiment, for the parameter set of ($\mu \cdot \tau_{CT} =10^{-10}$ cm^{2}V^{-1} or $\mu=10^{-2}$ cm^{2}s^{-1}V^{-1}, τ_{CT} =10 ns). Figure 7c shows the best fit of the functional form between the model's CT separation efficiency and the measured EQE, and Figure 7d shows the effective binding energy deduced from the data in Figure 7c, utilizing equation (12). Using this higher mobility, the quality of the fit improves as it holds well also at room temperature. Namely, the results presented in Figure 7c confirm that it is the instantaneous or "disorder-free" mobility that should be used in the Onsager-Braun expression.[45] In fact, only the use of the "disorder-free" mobility is consistent with our use of temperature independent mobility[47] to deduce κ_{cd} in the Onsager-Braun formalism.

The deduced junction disorder ($\sigma_{cp}=90$ meV, $\sigma_a=\sigma_d=65$ meV) is unchanged. However, the absolute values in Figure 7c are higher than those of Figure 7a. The absolute values, for the +0.5 V bias, indicate that at room temperature the CT separation efficiency is close to 100% implying that the charge generation efficiency, at room temperature, is almost bias independent. The deduction requires that the measured bias dependence of the IQE at room temperature would be largely a result of the
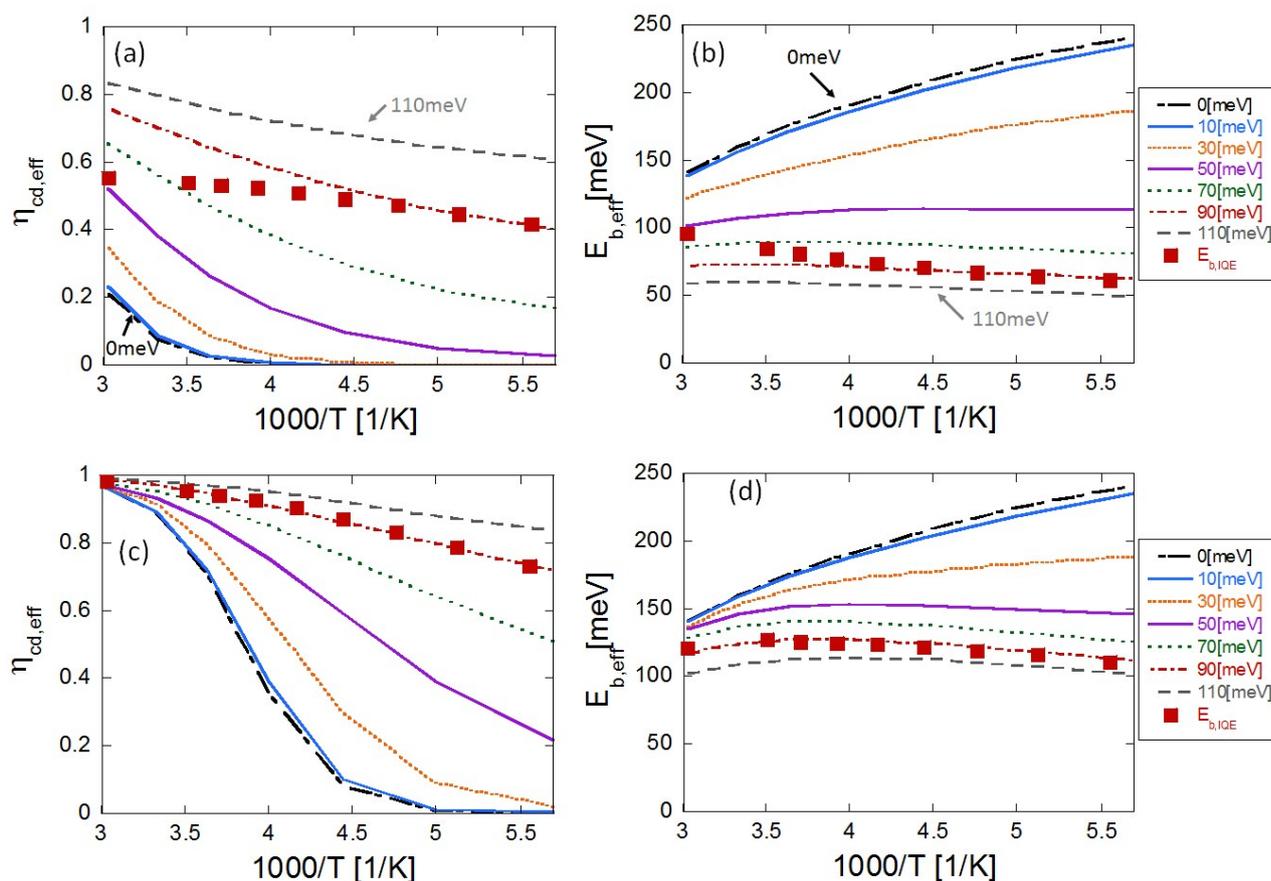

Figure 7. (a) and (b) For the simulated device we used $\mu=10^{-4}$ cm^{2}s^{-1}V^{-1} and τ_{CT} =10 ns: (a) Square red symbols are measured results for PTB7-th:ITIC device IQE as a function of 1000/T. Other lines are the simulation results for $\eta_{cd,eff}$ as a function of 1000/T for different disorder magnitudes. (b) Calculated $E_{b,eff}$ for both measurements and simulated results by using eq(12). (c) and (d) For the simulated device we used $\mu=10^{-2}$ cm^{2}s^{-1}V^{-1} and τ_{CT} =10 ns: (c) Square red symbols are measured results for PTB7-th:ITIC device IQE as a function of 1000/T. Other lines are the simulation results for $\eta_{cd,eff}$ as a function of 1000/T for different disorder magnitudes. (d) Calculated $E_{b,eff}$ for both measurements and simulated results by using eq(12).

trap-assisted recombination where the traps are mainly filled by dark injection. Similar conclusion was drawn from the discussion of Figure 6d and Figure 6e above.

The field independent exciton dissociation is in agreement with the observation of field independent charge generation in time-delayed collection field (TDCF) measurements of the same material system.[48] To further support the above conclusion, we performed a device simulation using the Sentaurus platform (by Synopsis). For the simulation parameters and fitting procedure see supplementary. Figure 8 shows the simulation's fits to measured data as well as the result when traps are neglected. The excellent fit between measured and simulated results supports the notion that the bias dependent QE is due to trap assisted recombination through traps that are mostly filled already in the dark (at room temperature). Namely, the EED model, the detailed experimental analysis, and the device model are self-consistent.

Discussion

We found that the experimentally measured internal quantum efficiency and the deduced binding energy can be reproduced by the theory presented above. To reach this point we started by modifying existing theories[19, 21] to come up with a model that is device-compatible. Formally, we were after including the spatial dispersion of the density of states[27] to produce device-equivalent effective medium. Within the EED model we examine the local energy landscape surrounding the CT exciton and represent this local environment by its CT dissociation efficiency and not by its local binding energy. Translating into the device level is then straight forward through arithmetic mean of the local efficiencies found throughout the device. We then use the Onsager-Braun expression to define a new binding energy which we term the device-equivalent effective binding energy. It describes the apparent energy required to dissociate CT-excitons within the non-homogenous device. We consider this approach to be our most important contribution as it allows direct comparison with relevant device characteristics. An attribute that was reserved to dynamic Monte-Carlo simulations.[15, 21] As the issue of binding energy is important we present in the supplementary a detailed analysis and comparison of three approaches of defining effective binding energy, in the context of entropy and disorder (Figure 7S). Using device-equivalent binding energy somewhat complements the discussion of what the actual binding energy is [15] and the importance of dimensionality[20] in determining its value.

As the dimensionality of the problem is important,[20] we decided to perform our calculations by actually generating a 3D lattice that represents the local environment and guides the calculation of the available sites to dissociate through ($\Omega(r)$). The discussion in the supplementary also compares using 3D lattice and not (Figure8S). However, we still use here a bi-layer morphology that could only be considered as a reasonable approximation to full BHJ morphology.[21] The sensitivity to fine morphological details is also addressed in the supplementary materials (Figure 1S to Figure 6S). For example, Figure 6S shows that if only the first interface layers are forced to be ordered,
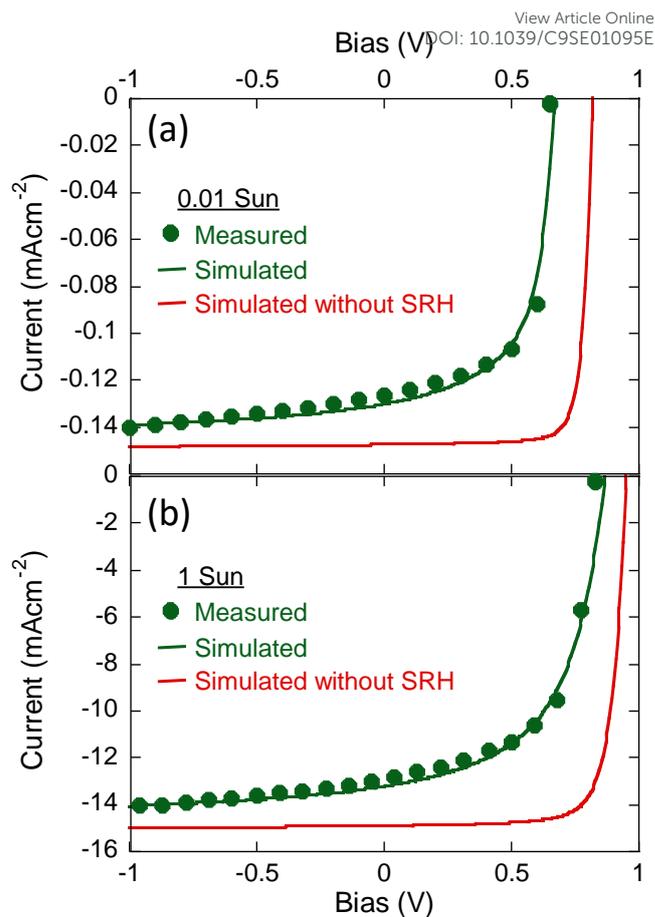
Figure 8. Measured and simulated J-V curves under 10^{-2} Sun (a) and 1 Sun (b) illumination. Symbols are the measured Data. Green line is the best fit achieved using C_pP_T=8 ns for the trap assisted (SRH) recombination and workfunction of ZnO being 0.22 eV below the LUMO. Red line is for bimolecular recombination only (10^{-12} cm^{3}s^{-1}). See text for other parameters used.

the binding energy distributions significantly narrows with respect to Figure 4.

To test if our implementation of the EED model is good-enough, to describe and analyze working devices, we compared its prediction to results obtained through detailed NFA device analysis. As the EED model deals only with charge generation we expanded the theoretical scope and included a semiconductor device model. The self-consistency between the EED model, the experiments, and the device simulations indicates that our implementation of the EED model is good enough to explain device data like the one reported here. Figure 7a,b and Figure 7c,d were calculated for two values of $\mu \cdot \tau_{CT}$. To complete the picture, Figure 9S shows the dissociation efficiency as a function of $\mu \cdot \tau_{CT}$ or $\kappa_{cd} \cdot \tau_{CT}$. From such results we can infer that the quality of the fit improves significantly already at $\mu \cdot \tau_{CT}$ =10^{-9}. The good fit (Figure 7) suggests that entropy and disorder govern the exciton dissociation in the PTB7-Th:ITIC BHJ OPV device.

Conclusions

We presented a new EED model and an intuitive definition for CT binding energy that is relevant to operating BHJ OPVs. This

definition maintains the distinction from the activation energy of the charge generation[10, 15] and results in E_{beff} of slightly above 100meV, which is in agreement with a recent report[49] probing this quantity in NFA OPV. Performing direct comparison with relevant experimental data allow us to conclude that entropy and disorder is not only an optional explanation but rather that it dominates the CT exciton dissociation in the measured device. We found that a bulk disorder of only σ=70meV is sufficient to dissociate the excitons. Avoiding disorder of about 70 meV in a BHJ structure is very difficult and our work may help in explaining why high charge generation efficiency is so common for NFA devices, even though low energy offset between donor and acceptor materials is maintained. We note that σ=70 meV is a low enough disorder value that by itself is not supposed to preclude steady state mobilities as high as 10^{-2} $cm^2V^{-1}s^{-1}$ (assuming disorder-free mobility of 1 $cm^2V^{-1}s^{-1}$).

Our device analysis (supplementary figure 14s and 15s) suggests that on the device side one should make use of blocking layers[50] that allow for electrostatic band bending that would increase the built in potential under light excitation.[51, 52] However, this is outside the scope of this paper.

Experimental

Device Fabrication

Organic solar cells were fabricated with the following structure: ITO/zinc oxide (ZnO)/active layer/molybdenum trioxide (MoO_3)/silver (Ag). The ITO glass was pre-cleaned in an ultrasonic bath of acetone and isopropanol, and treated in ultraviolet–ozone chamber (Jelight Company, USA) for 15 min. A thin layer (30 nm) of ZnO sol-gel was spin-coated onto the ITO glass and baked at 200 °C for 60 min. A mixture of PTB7-Th (One-Materials Inc)/ITIC (Solarmer Inc) was dissolved in DCB (Sigma-Aldrich Inc) solvent (D:A = 1:1.5, 15 mg mL^{-1} in total) with stirring overnight (80 °C). Then, the blended solution was spin-coated on the ZnO layer to form a photosensitive layer. The thickness of active layer was ≈100 nm. A MoO_3 (≈10 nm) and Ag layer (≈100 nm) was then evaporated onto the surface of the photosensitive layer under vacuum (≈10–5 Pa) to form the back electrode. The active area of the device was 0.1 cm^2.

Measurements procedure

Current-voltage characteristics was measured with a Keithley 2612 source meter. Spectrally resolved external quantum efficiency (EQE) was performed in the following way. Light from a tungsten halogen lamp (Oriel, 250 W QTH) was dispersed through a monochromator (Oriel, CS130). The light intensity was monitored using reference silicon and germanium photodetectors. Light from the monochromator (1.5 µWcm^{-2} at 600 nm) was chopped at 120 Hz and the signal was read using a lock-in amplifier (EG&G 7265). Power dependent quantum efficiency was measured using a white light emitting diode metrics, whose intensity was controlled by the bias current. Appropriate optical density (OD) filters were used to extend the

intensity range (~5 order) from ultra-low to more than one sun light intensity. Care was taken to ensure that the light spot falls within the pixel to avoid any potential edge effects. The temperature was controlled by a low temperature micro probes and a K-20 controller (MMR technologies Inc). IQE was deduce by reflection measurement in the range of 400-1000 nm (Agilent Cary 5000) with a theta-2 theta configuration at an angle of 6 deg.

Conflicts of interest

There are no conflicts to declare.

Acknowledgements

Notes and references

1. P. Cheng, G. Li, X. Zhan and Y. Yang, *Nature Photonics*, 2018, **12**, 131-142.
2. W. Zhao, S. Li, H. Yao, S. Zhang, Y. Zhang, B. Yang and J. Hou, *Journal of the American Chemical Society*, 2017, **139**, 7148-7151.
3. X. Che, Y. Li, Y. Qu and S. R. Forrest, *Nature Energy*, 2018, **3**, 422-427.
4. S. Li, W. Liu, M. Shi, J. Mai, T.-K. Lau, J. Wan, X. Lu, C.-Z. Li and H. Chen, *Energy & Environmental Science*, 2016, **9**, 604-610.
5. J. Hou, O. Inganäs, R. H. Friend and F. Gao, *Nature Materials*, 2018, **17**, 119.
6. K. Li, Y. Wu, Y. Tang, M.-A. Pan, W. Ma, H. Fu, C. Zhan and J. Yao, *Adv. Energy Mater.*, 2019, **0**, 1901728.
7. L. Meng, Y. Zhang, X. Wan, C. Li, X. Zhang, Y. Wang, X. Ke, Z. Xiao, L. Ding, R. Xia, H.-L. Yip, Y. Cao and Y. Chen, *Science*, 2018, **361**, 1094.
8. R. A. J. Janssen and J. Nelson, *Advanced Materials*, 2013, **25**, 1847-1858.
9. D. Liraz, H. Shekhar, L. Tzabari and N. Tessler, *The Journal of Physical Chemistry C*, 2018, **122**, 23271-23279.
10. C. L. Braun, *The Journal of Chemical Physics*, 1984, **80**, 4157-4161.
11. A. B. Matheson, S. J. Pearson, A. Ruseckas and I. D. W. Samuel, *The Journal of Physical Chemistry Letters*, 2013, **4**, 4166-4171.

12. S. Gélinas, A. Rao, A. Kumar, S. L. Smith, A. W. Chin, J. Clark, T. S. van der Poll, G. C. Bazan and R. H. Friend, *Science*, 2014, **343**, 512.

13. V. I. Arkhipov, P. Heremans and H. Bässler, *Applied Physics Letters*, 2003, **82**, 4605-4607.

14. B. Bernardo, D. Cheyns, B. Verreet, R. D. Schaller, B. P. Rand and N. C. Giebink, *Nature Communications*, 2014, **5**, 3245.

15. S. Athanasopoulos, F. Schauer, V. Nádaždy, M. Weiß, F.-J. Kahle, U. Scherf, H. Bässler and A. Köhler, *Advanced Energy Materials*, 2019, **9**, 1900814.

16. T. Vehoff, B. Baumeier, A. Troisi and D. Andrienko, *Journal of the American Chemical Society*, 2010, **132**, 11702-11708.

17. J. C. Blakesley and D. Neher, *Physical Review B*, 2011, **84**, 075210.

18. J. D. Zimmerman, X. Xiao, C. K. Renshaw, S. Wang, V. V. Diev, M. E. Thompson and S. R. Forrest, *Nano Letters*, 2012, **12**, 4366-4371.

19. S. N. Hood and I. Kassal, *The Journal of Physical Chemistry Letters*, 2016, **7**, 4495-4500.

20. B. A. Gregg, *The Journal of Physical Chemistry Letters*, 2011, **2**, 3013-3015.

21. E. Kawashima, M. Fujii and K. Yamashita, *Journal of Photochemistry and Photobiology A: Chemistry*, 2019, **382**, 111875.

22. T. M. Clarke and J. R. Durrant, *Chemical Reviews*, 2010, **110**, 6736-6767.

23. J. L. Bredas, J. Cornil and A. J. Heeger, *Adv. Mater.*, 1996, **8**, 447.

24. L. Onsager, *The Journal of Chemical Physics*, 1934, **2**, 599-615.

25. L. Onsager, *Physical Review*, 1938, **54**, 554-557.

26. K. A. Connors, *Chemical kinetics: the study of reaction rates in solution*, John Wiley & Sons, 1990.

27. N. Rappaport, Y. Preezant and N. Tessler, *Phys. Rev. B*, 2007, **76**, 235323.

28. N. Rappaport, O. Solomesch and N. Tessler, *J. Appl. Phys.*, 2006, **99**, 064507.

29. A. Devižis, J. De Jonghe-Risse, R. Hany, F. Nüesch, S. Jenatsch, V. Gulbinas and J.-E. Moser, *Journal of the American Chemical Society*, 2015, **137**, 8192-8198.

30. H. van Eersel, R. A. J. Janssen and M. Kemerink, *Adv. Funct. Mater.*, 2012, **22**, 2700-2708.

31. C. Groves, R. A. Marsh and N. C. Greenham, *J. Chem. Phys.*, 2008, **129**, 114903.

32. M. Wojcik, P. Michalak and M. Tachiya, *Bull. Korean Chem. Soc.*, 2012, **33**, 795-802.

33. S. Athanasopoulos, S. Tscheuschner, H. Bässler and A. Köhler, *J. Phys. Chem. Lett.*, 2017, **8**, 2093-2098.

34. X. Yi, B. Gautam, I. Constantinou, Y. Cheng, Z. Peng, E. Klump, X. Ba, C. H. Y. Ho, C. Dong, S. R. Marder, J. R. Reynolds, S.-W. Tsang, H. Ade and F. So, *Advanced Functional Materials*, 2018, **28**, 1802702.

35. L. Zhang, B. Lin, Z. Ke, J. Chen, W. Li, M. Zhang and W. Ma, *Nano Energy*, 2017, **41**, 609-617.

36. S. Shoaee, M. Stolterfoht and D. Neher, *Advanced Energy Materials*, **0**, 1703355.

37. S. Zhang, L. Ye, W. Zhao, D. Liu, H. Yao and J. Hou, *Macromolecules*, 2014, **47**, 4653-4659.

38. Y. Lin, J. Wang, Z.-G. Zhang, H. Bai, Y. Li, D. Zhu and X. Zhan, *Adv. Mater.*, 2015, **27**, 1170-1174.

39. N. Rappaport, O. Solomesch and N. Tessler, *J. Appl. Phys.*, 2005, **98**, 033714.

40. L. Tzabari, J. Wang, Y.-J. Lee, J. W. P. Hsu and N. Tessler, *The Journal of Physical Chemistry C*, 2016, **120**, 10146-10155.

41. L. Tzabari, J. Wang, Y.-J. Lee, J. W. P. Hsu and N. Tessler, *The Journal of Physical Chemistry C*, 2014, **118**, 27681-27689.

42. U. Würfel and M. Unmüssig, *Solar RRL*, 2018, **2**, 1800229.

43. X. Song, N. Gasparini and D. Baran, *Advanced Electronic Materials*, 2018, **4**, 1700358.

44. B. Ebenhoch, S. A. J. Thomson, K. Genevičius, G. Juška and I. D. W. Samuel, *Organic Electronics*, 2015, **22**, 62-68.

45. D. A. Vithanage, A. Devižis, V. Abramavičius, Y. Infahsaeng, D. Abramavičius, R. C. I. MacKenzie, P. E. Keivanidis, A. Yartsev, D. Hertel, J. Nelson, V. Sundström and V. Gulbinas, *Nat. Commun.*, 2013, **4**, 2334.

46. W. F. Pasveer, J. Cottaar, C. Tanase, R. Coehoorn, P. A. Bobbert, P. W. M. Blom, D. M. de Leeuw and M. A. J. Michels, *Physical Review Letters*, 2005, **94**, 206601.

47. N. Tessler, Y. Preezant, N. Rappaport and Y. Roichman, *Adv. Mater.*, 2009, **21**, 2741-2761.

48. D. Baran, *Private Communication*, 2019.

49. Y. Dong, H. Cha, J. Zhang, E. Pastor, P. S. Tuladhar, I. McCulloch, J. R. Durrant and A. A. Bakulin, *J. Chem. Phys.*, 2019, **150**, 104704.

50. W. Peter, *Physics of Solar Cells*, Wiley, 2005.

51. O. Magen and N. Tessler, *J. Appl. Phys.*, 2016, **120**, 194502.

52. N. Tessler, *J. Appl. Phys.*, 2015, **118**, 215501.

Supplementary materials

Translating Local Binding Energy to a Device Effective one

Dan Liraz,[1] Pei Cheng,[2] Yang Yang,[2] Nir Tessler[1]

[1] Microelectronic & Nanoelectronic Centers, Electrical Engineering Department, Technion
Israel Institute of Technology, Haifa (Israel)
[2]   Department of Materials Science and Engineering, University of California, Los Angeles,
CA, USA

1. Calculating Ω(r)

Our method of counting is described in the paper. In this section, we give some counting result for different morphologies.

2. Morphology/Geometry

First, we describe the simplest morphology. Consider a symmetrical (the morphology of donor and acceptor is identical), device, with cubic lattice, with lattice parameter of 1[nm]. The 2D analog situation is shown in Figure 1S. Point 'j' is located at the origin. The colored area represents sites which are part of r-separated pair-configuration. Note that a colored site may participate in multiple r-separated pair-configuration.
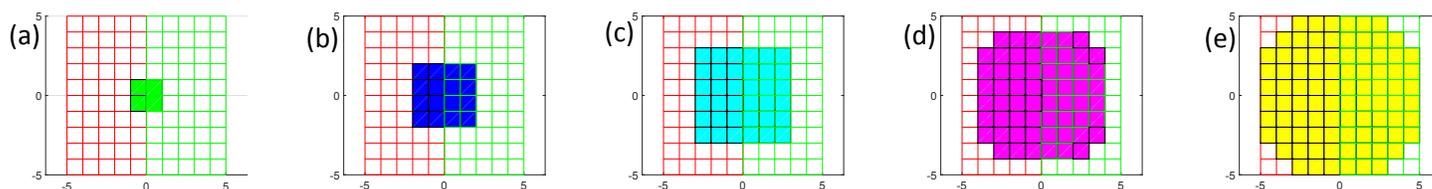
Figure 1S. 2D illustration of simple morphology. Red mesh describes sites on side A and green mesh – side B. Point 'j' is located at the origin. The colored area represents sites which taking place in forming r-separated CT. graphs (a)-(e) present the feeding area for r-separated CTs, where r is equal to 1-5[nm] respectively

Second, replace one side cubic lattice with elongated shaped sites, 'face-on' conformation, represented by 1X4X1 cuboid. we use Cartesian coordinate system (x, y, z), when the x-axis is perpendicular to donor-acceptor interface and y, z axes are parallel to it. The 2D analog situation is shown in Figure 2S.
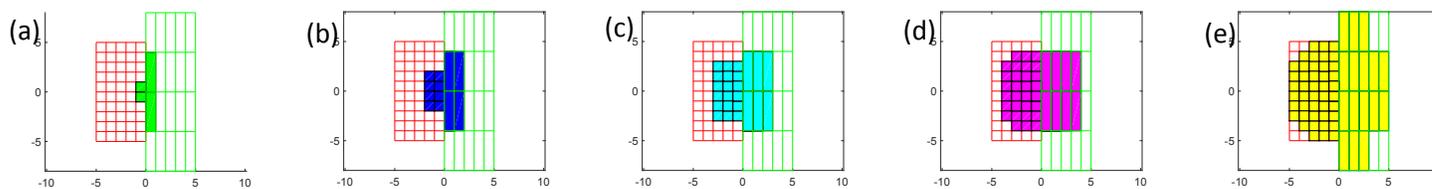

Figure 2S. 2D illustration of sites with elongated shape morphology, 'face-on' conformation (compare to Figure 1S).

Third, similar to second case, but instead consider 'edge-on' conformation. 2D analog situation is shown in Figure 3S.
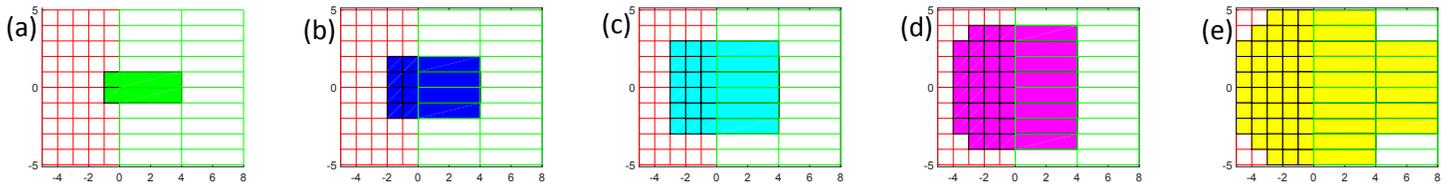

Figure 3S. 2D illustration of sites with elongated shape morphology, 'edge-on' conformation (compare to Figure 2S and Figure 1S).

Fourth, examine more elongated (1X10X1) 'face-on' system.

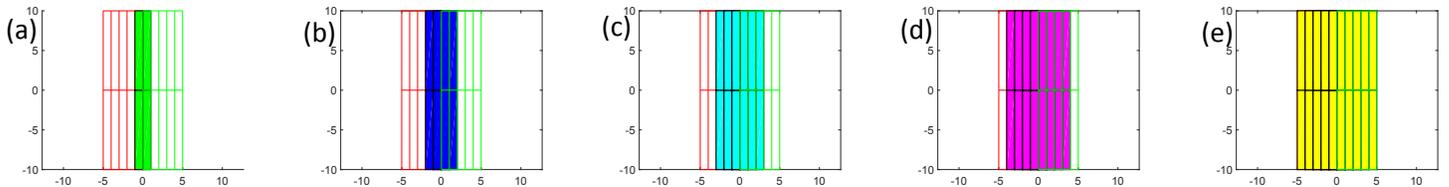Fifth is a parallel 'face-on':'face-on' system represented by 1X10X1:1X10X1 cuboids (Figure 4S).

Figure 4S. 2D illustration parallel 'face-on':'face-on' system (compare to Figure 1S).

Sixth is a perpendicular 'face-on':'face-on' system represented by 1X10X1:1X1X10 cuboids (Figure 5S).
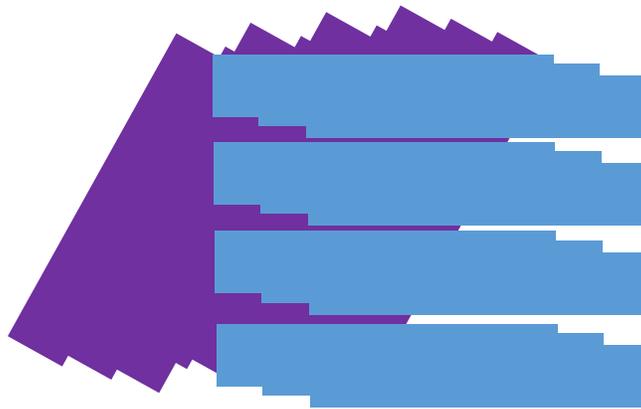
Figure 5S. 3D illustration of a perpendicular 'face-on':'face-on' system (compare to Figure 4S).

Seventh is a 'face-on':'edge-on' system represented by 1X10X1:10X1X1 cuboids

Eighth is a 1X1X1:3X3X3 system.

Ninth is a 1X6X10:3X3X3 system.

For each morphology, we calculated Ω as a function of r and extracted its figure of merit. Table 1S organizes the counting results.

Number	dimensions	Figure of merit	a	R^3
1	1X1X1:1X1X1	$a \cdot r^3$	2.27±0.03	0.999
2	1X1X1:1X4X1	$a \cdot r^3$	1.94±0.02	0.999
3	1X1X1:4X1X1	$a \cdot r^3$	1.94±0.02	0.999
4	1X1X1:1X10X1	$a \cdot r^3$	1.89±0.01	1.000
5	1X10X1: 1X10X1	$a \cdot r^3$	1.39±0.01	1.000
6	1X10X1: 1X1X10	$a \cdot r^3$	1.40±0.01	1.000
7	1X10X1: 10X1X1	$a \cdot r^3$	1.40±0.01	1.000
8	1X1X1:3X3X3	$a \cdot r^3$	1.52±0.01	1.000
9	1X6X10:3X3X3	$a \cdot r^3$	0.73±0.02	0.995

Table 1S. counting Ω(r) for diverse morphology

We conclude, that although the result is always proportional to r^3, the pre-factor may change by a factor of up to three depending on the morphology.

3. Ordered interfacial layer

We simulated the case when the first interfacial layers of the donor and acceptor are ordered. All other molecules are energetic disordered with Gaussian distribution, the width of this distribution is according to the graph legend. We apply the EED model on a cubic geometry with lattice constant of 1 nm and assume ε=3.3.

Compare these narrow local binding energy distributions to the results of the fully disordered system (Figure 4 a and b).
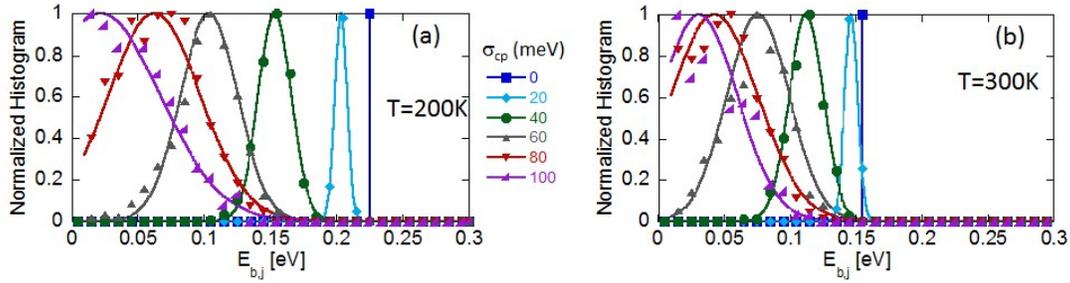
Figure 6S. a) and (b) are the normalized distributions of the local binding energy ($E_{b,j}$) at 200 °K and at 300 °K, respectively. Symbols are the simulation results and solid lines are Gaussian fits. Blue, cyan, green, grey, red, and magenta lines are simulation results for junction disorder standard deviation (σ_{cp}) of 0 meV, 20 meV, 40 meV, 60 meV, 80 meV, and 100 meV, respectively.

4. Dissociation efficiency and binding energy

We have presented a model that accounts for the effect of entropy on CT exciton dissociation in the presence of disorder. Our work builds on the paper by Hood et. al. [1] but the translation of the disordered film to an effective medium is very different. The importance of choosing the most suitable method to "average" the disordered medium to obtain an effective (device equivalent) value has been discussed extensively in the context of charge mobility.[2, 3] Starting our work we could consider three methods of treating entropy and disorder, one of which was used in the main paper. The three methods (Figure 7) start with realizing that the sample should be considered as being composed of different environments (labeled j), each having its own set of disordered energy states and a resulting thermodynamic potential, $\Delta F_j(r)$. The following task is to translate the ensemble of ΔF_j into an effective quantity. The first rigorous treatment of entropy and disorder was by Hood et. al. [1] and in Figure 7 it is depicted as method A. The process of creating the effective, or device equivalent, medium consists of averaging the thermodynamic potentials and using the average potential (ΔF_{eff}) to extract the effective binding energy (see Figure 1 in the main text). The effective binding energy drops to below kT at junction disorder above $\sigma_{cp} =$ 130meV or bulk disorder of $\sigma_a=\sigma_d=90$meV (Figure 8s). Linking this binding energy to device properties is not straight forward as a binding energy below kT would result in 100% dissociation efficiency regardless of any other material's parameters (as exciton lifetime or charge hopping rate).
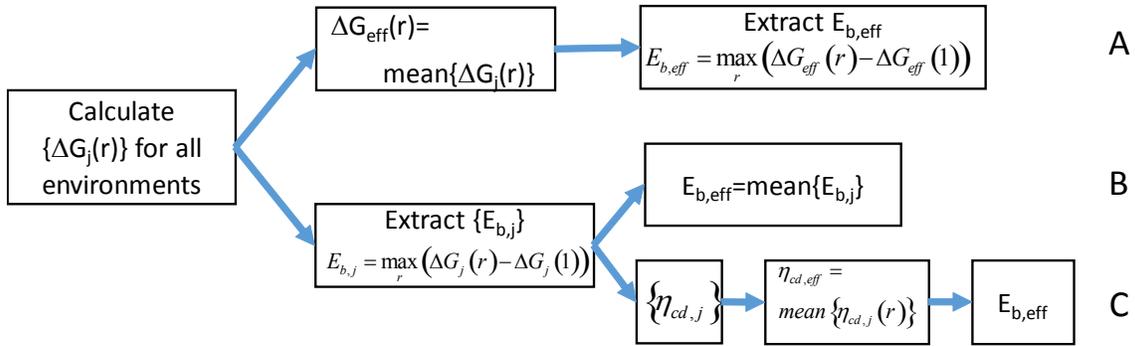
Figure 7S. Illustration of three methods to arrive at an effective binding energy

In Figure 4 we showed that if one does not average ΔF_j but rather extract from every j environment its local binding energy (E_{bj}) and separation distance, than the results have a rather large distribution. As all distributions, in Figure 4, are fitted well by a gaussian it may trigger what we labeled as method B in Figure 7S. Namely, define the effective binding energy as the average, or most probable, binding energy. Using this method, the effective binding energy drops slower, relative to A, as a function of disorder (Figure 8s). However, it also does not lend itself for direct comparison with experimental data. The third method (C in Figure 7) is the one proposed here. The basic idea behind it is to try and mimic the physical process taking place in the solar cell device. Namely, the dissociation efficiency of a device is a result of collecting the charges that were generated at different positions within the layer (i.e. at different environments).

In Figure 8s we compare results obtained by the three methods as well as the effect of the counting strategy. As methods A and B do not provide the effective dissociation efficiency, we compare the binding energies. The top raw of Figure 8s was produced as in the main paper. For each environment to be evaluated, first a 3D lattice of sites energies is generated and then Ω for all 'r' are computed using the same lattice. As the same lattice is used for all 'r' there is some correlation between them. The second and third raw use the method as in ref [1] where for every 'r' one generates a new set of states with their number dictated by the rule ($\Omega=2r^3$ or $\Omega=r^3$).
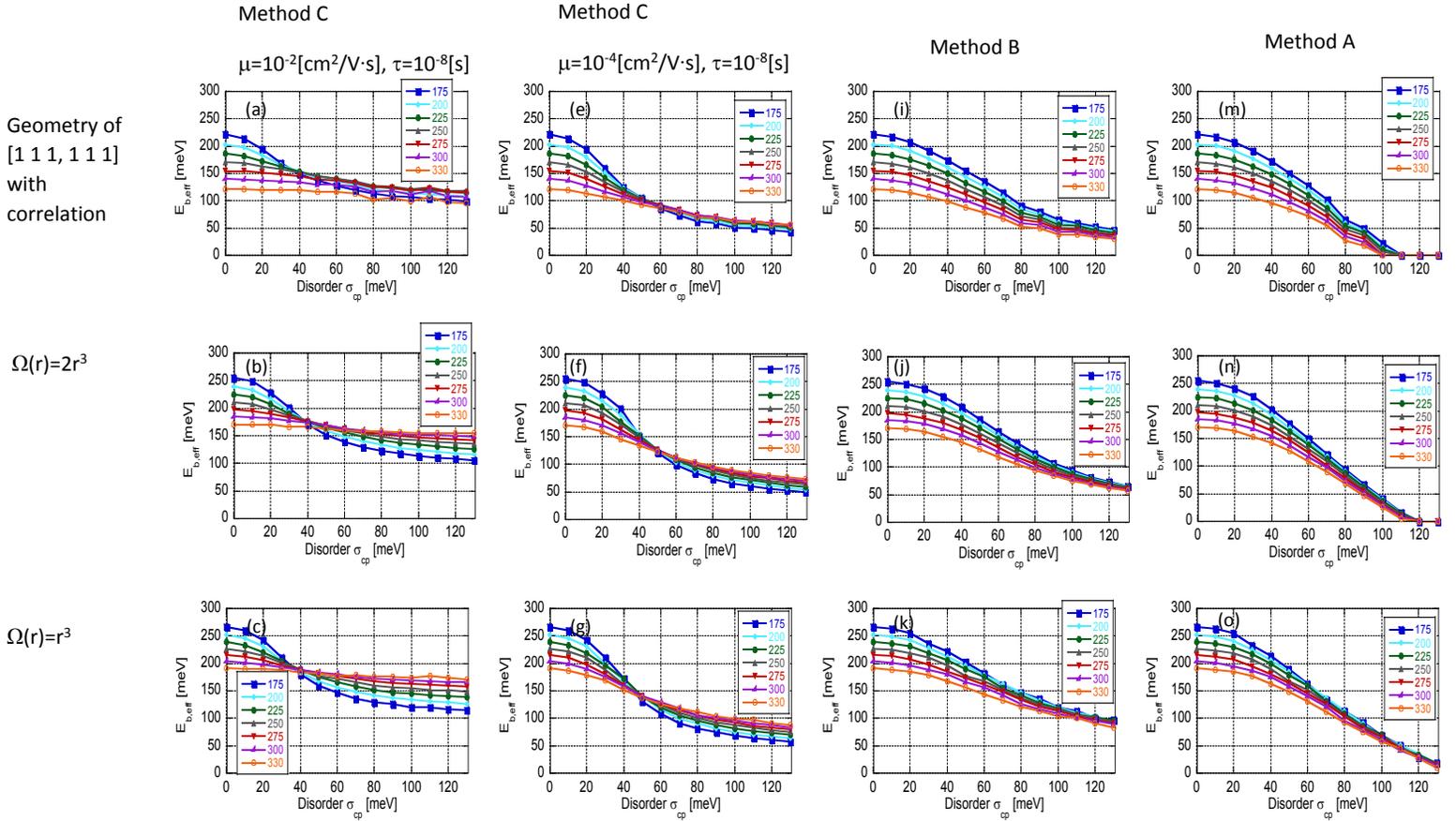
Figure 8S. $E_{b,eff}$ *versus disorder for all three methods. (a-c) Method A $\mu=10^{-2}[cm^2/V{\cdot}s]$, $\tau_{CT}=10^{-8}[sec]$; (e-g) Method A $\mu=10^{-4}[cm^2/V{\cdot}s]$, $\tau_{CT}=10^{-8}[sec]$; (i-k) Method B; (m-o) Method C. (a, e, i, m) calculating G(r) while scanning the geometry of [1 1 1, 1 1 1] (with correlation); (b, f, j, n) $\Omega(r)=2\pi r^3/3$ no correlation; (c, g, k, o) $\Omega(r)= r^3$ no correlation*

First, we discuss differences between results of method A and method B. As long as all CTs dissociate in the same separation distance, method A and B lead to identical results. Thus both methods predict the same $E_{b,eff}$ for low disorder when almost all CT dissociates at the same separation distance. But as the disorder grows, the distribution of dissociation distance becomes wider, each $\Delta F_j(r)$ has maximum at a different r, and by averaging $\Delta F_j(r)$ the maximum value, $E_{b,eff}$, is lowered. Method A produces a fast decreasing $E_{b,eff}$ reaching zero within the disorder range considered. Method B also shows that $E_{b,eff}$ is decreasing, but in a more softened way.

For Method C we use two columns as this method takes into account the materials' physical properties as the exciton lifetime and the mobility (hooping rate). For the two mobilities used we note that the effective binding energy does not reduce to zero. Moreover, at high disorder the temperature dependence flips sign instead of gradually diminishing to zero. The most unique

feature of method C can not be presented in a figure like Figure 8s as it is the only method that directly evaluates the device equivalent effective dissociation efficiency.

5. Further discussion regarding $\eta_{cd,eff}$ and $E_{b,eff}$ dependencies

Figure 9S shows the effective dissociation efficiency at (a) 200[^{0}K] and at (b) 300[^{0}K]. $\kappa_{cd}\tau_{CT}$ range is matched to mobility range of 10^{-5}-10^{-2}[cm^2/V·s], assuming τ_{CT} =10ns. As $\kappa_{cd}\tau_{CT}$ grows, so does the dissociation efficiency as the hopping away (κ_{cd}) becomes faster relative to the decay. In case of ordered or close to an ordered system, the dissociation efficiency is a linear function of $\kappa_{cd}\tau_{CT}$. We may explain this linearity by paying attention to the fact that dissociation rate is respectively low because in the ordered case, unlike the disordered case, all $E_{b,j}$ share almost the same value and it is unlikely to find low $E_{b,j}$. According to eq(11), when dissociation rate is low, $\eta_{cd,eff}$ is a linear function of $\kappa_{cd}\tau_{CT}$:

$$\eta_{cd,eff} = \left\langle \frac{\kappa_{cd}\tau_{CT}\exp\left(-\dfrac{E_{b,j}}{k_bT}\right)}{\kappa_{cd}\tau_{CT}\exp\left(-\dfrac{E_{b,j}}{k_bT}\right)+1} \right\rangle_j \xrightarrow[\kappa_{cd}\exp\left(-\frac{E_{b,j}}{k_bT}\right)?\,\frac{1}{\tau_{CT}}]{} \kappa_{cd}\tau_{CT}\left\langle\exp\left(-\frac{E_{b,j}}{k_bT}\right)\right\rangle$$

The dissociation is more effective as the disorder is increases because the expectation value of $E_{b,j}$ drops as the disorder increases. Naturally, high temperature is another factor that encourages dissociation and leads to high $\eta_{cd,eff}$.
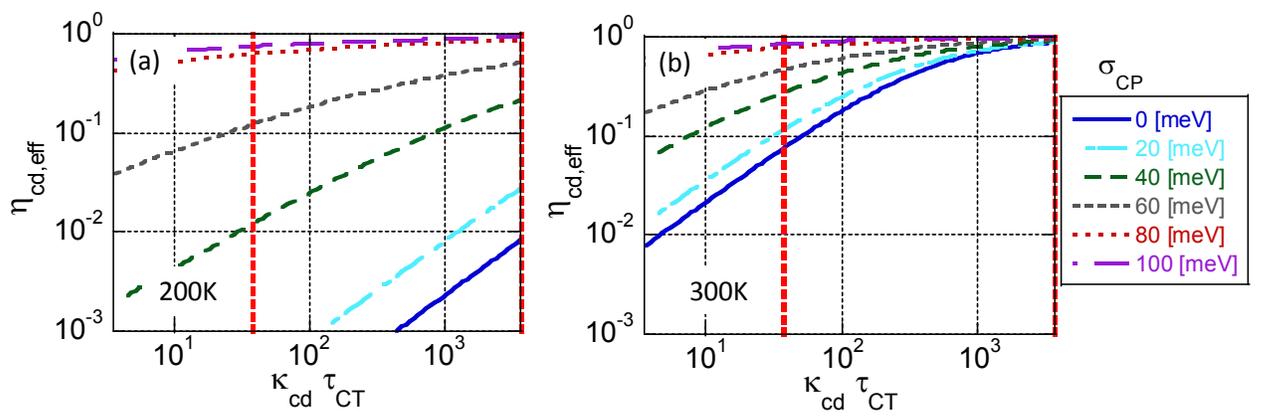
Figure 9S. effective dissociation efficiency ($\eta_{cd,eff}$) as function of $\kappa_{cd}\tau_{CT}$ for various junction disorder standard deviations (a) at 200[K] and at (b) 300[K]. The vertical dashed lines correspond to $\mu=10^{-4}$cm^{2}v^{-1}s^{-1} (left line) and $\mu=10^{-2}$cm^{2}v^{-1}s^{-1} (right edge line) used for Figure 7 in the main text.

As we deduce $E_{b,eff}$ from $\eta_{cd,eff}$, $E_{b,eff}$ inherits $\eta_{cd,eff}$ temperature, disorder, and $\kappa_{cd}\tau_{CT}$ dependencies. The fact $E_{b,eff}$ is $\kappa_{cd}\tau_{CT}$ dependent shows the insignificance of $E_{b,eff}$ as a key parameter in understanding the dissociation process.

The $\kappa_{cd}\tau_C$ dependence of $E_{b,eff}$ is shown in Figure 10S Again, $\kappa_{cd}\tau_{CT}$ range is matched to mobility range of 10^{-5}-10^{-2}[cm^2/V·s]. For the ordered case, $E_{b,eff}$ is independent of $\kappa_{cd}\tau_{CT}$ and equals to $E_{b,j}$ which are identical for any j.

It seems that the same conditions which support $\eta_{cd,eff}$ linear dependent on $\kappa_{cd}\tau_{CT}$ are responsible for $E_{b,eff}$ independent of $\kappa_{cd}\tau_{CT}$. We may verify this suspicion by using eq(12) and assuming

$$\eta_{cd,eff} \approx \kappa_{cd}\tau_{CT}\left\langle \exp\left(-\frac{E_{b,j}}{k_bT}\right)\right\rangle_j \text{ and } \eta_{cd,eff} <<1 (\text{dissociation rate is low}):$$

$$E_{b,eff} = -k_bT\left[\ln\left(\frac{\eta_{cd,eff}}{(1-\eta_{cd,eff})}\right)+\ln\left(\frac{k_{decay}}{\kappa_{cd}}\right)\right] \approx -k_bT\left[\ln\left(\frac{\eta_{cd,eff}}{\kappa_{cd}\tau_{CT}}\right)\right] \approx -k_bT\left[\ln\left(\left\langle\exp\left(-\frac{E_{b,j}}{k_bT}\right)\right\rangle_j\right)\right]$$

As $\kappa_{cd}\tau_{CT}$ and disorder are increasing, the assumptions are not holding and $E_{b,eff}$ becomes more
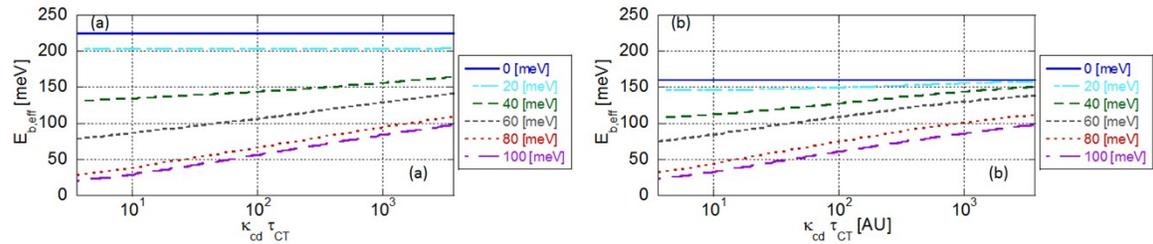

Figure 10S. Effective binding energy as a function of $\kappa_{cd}\tau_{CT}$ for various disorder standard deviations (a) at 200[K] and at (b) 300[K].

$\kappa_{cd}\tau_{CT}$ dependent.

`Figure 9S reveals that as $\kappa_{cd}\tau_{CT}$ is growing, $\eta_{cd,eff}$ tend to unity and all graphs of different disorders are getting closer together. This is the reason for the effect we see in Figure 10S causing all graphs getting closer together as $\kappa_{cd}\tau_{CT}$ increases.

Below we show the same results but where the x-axis is the junction (charge-pair) disorder and the curves are for different charge mobility values (translated to Kcd using Onsager-Braun theory).
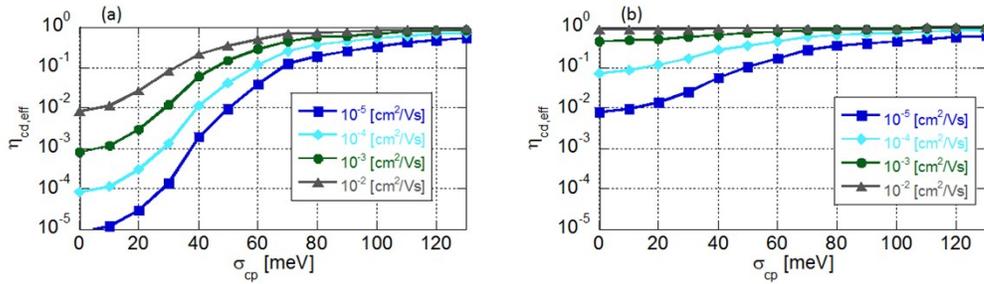

Figure 11S. effective dissociation efficiency as a function of disorder standard deviation for various values of $\kappa_{cd}\tau_{CT}$ (κ_{cd} values correlates to the mobility values written in the legend, $\tau_{CT}=10^{-8}[s]$) (a) at 200[K] and at (b) 300[K].at (b)
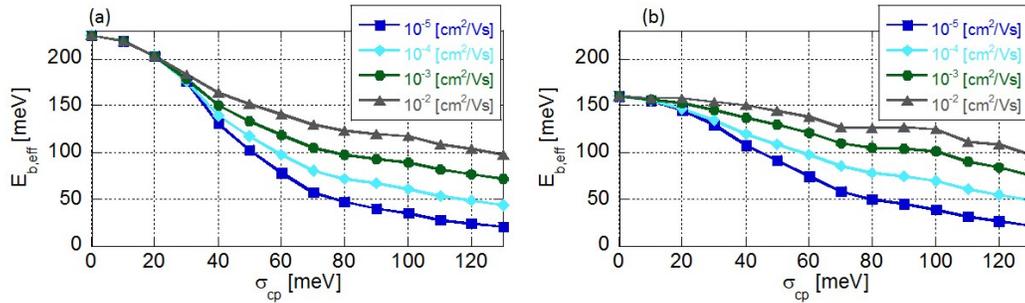

Figure 12S. effective binding energy as a function of disorder standard deviation for various values of (κ_{cd} values correlates to the mobility values written in the legend, $\tau_{CT}=10^{-8}[s]$) (a) at 200[K] and at (b) 300[K].
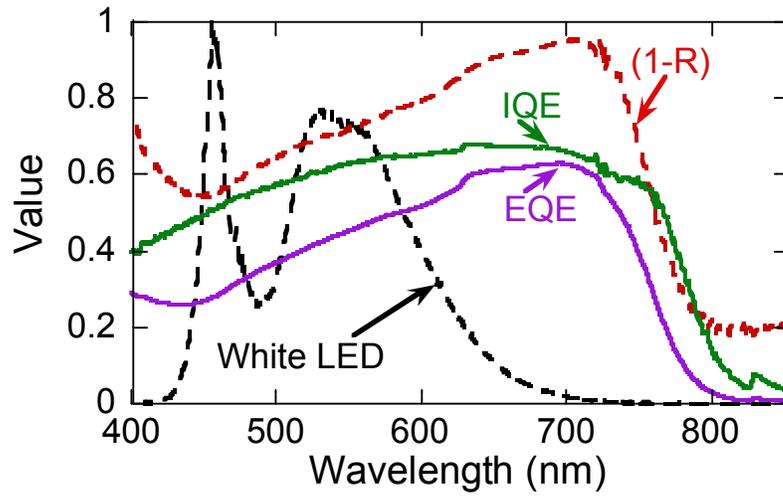
6. EQE and IQE

Figure 13s. Spectral distribution of the external quantum efficiency (EQE, purple), internal quantum efficiency (IQE, green), the absorbed fraction as 1 minus the measured cell's reflection (dashed red), the white LED (dashed, black)

The internal quantum efficiency is calculated by dividing the external quantum efficiency (EQE) by the fraction of light absorbed by the cell (1-R).

7. Device simulation data

For parameters we used the effective bandgap of 1.5 eV (deduced from the inset to Figure 6c in main text), disorder parameter for the HOMO and LUMO levels of σ=70 meV, $\mu_e = \mu_h = 2 \cdot 10^{-4}$ $cm^2v^{-1}s^{-1}$, and a low bimolecular recombination of 10^{-12} cm^3s^{-1} (Langevin coefficient is $2 \cdot 10^{-10}$ cm^3s^{-1}). For the contacts we assumed that the MoO_x has the potential to align with the HOMO level. We used the workfunction of the Zinc Oxide and the trap recombination lifetime (C_pP_T) as fitting parameters to fit the V_{OC} as well as the J-V shape at 1 Sun and 10^{-2} Sun. Best fits (Figure 8 in main text) were achieved using mid-gap traps with recombination lifetime of C_pP_T=8 ns and workfunction of ZnO being 0.22 eV below the LUMO level (of ITIC). Below we add two figures to expand the physical picture captured by the semiconductor device model.
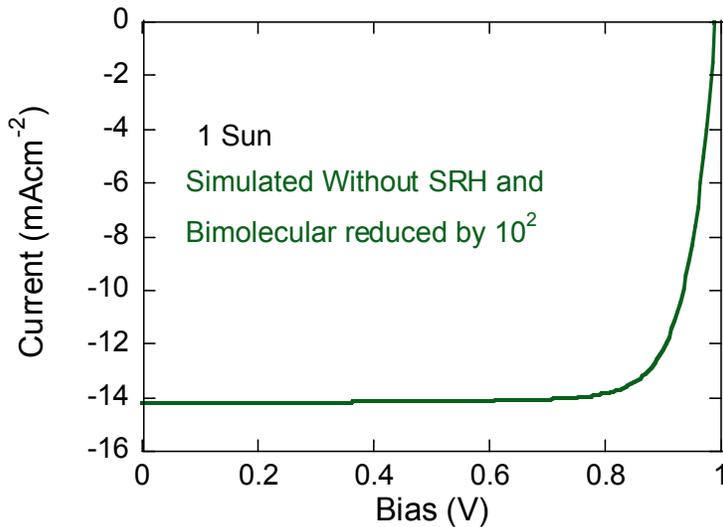

Figure 14s. Simulation of the same device as in the main paper but without trap-assisted recombination and the bimolecular recombination reduced by a factor of 100. The Result indicates that V_OC is limited to below 1V and not by the magnitude of the recombination losses but rather the build in voltage..
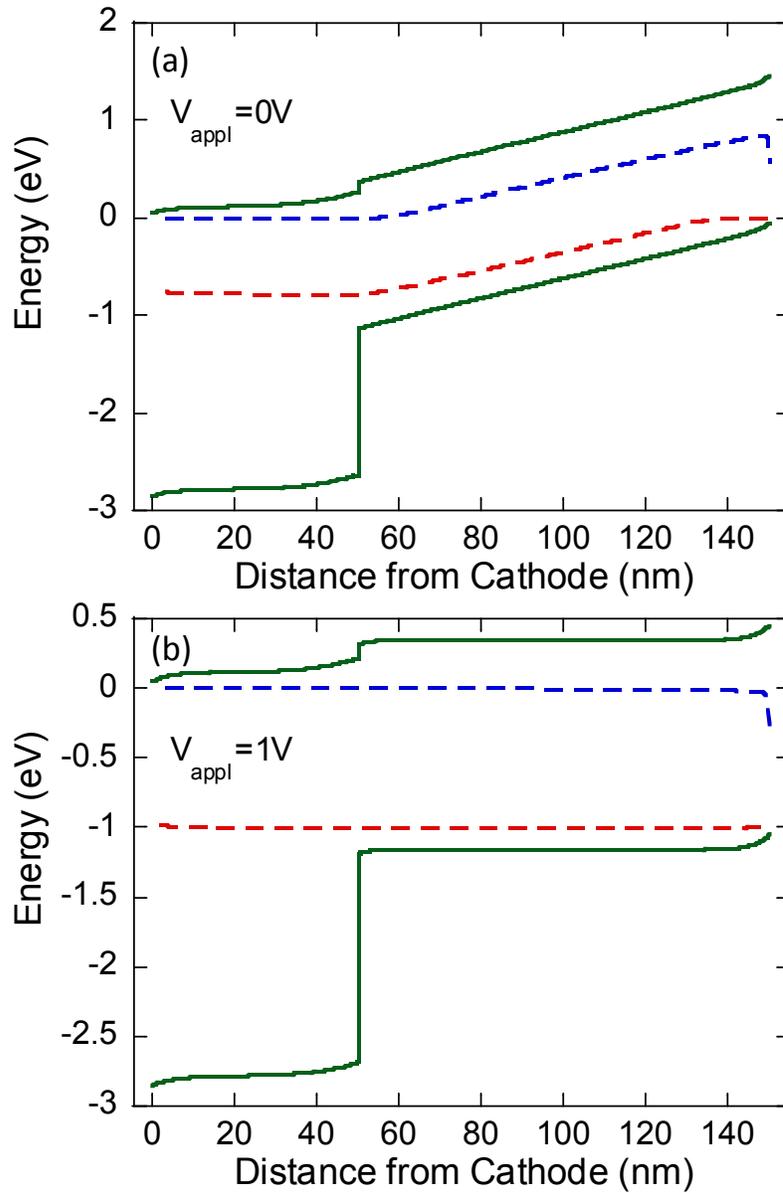
Figure 15s. Band structure of the same device simulated in Figure 14s under 1 Sun excitation. The dashed blue and red lines denote the electron and hole quasi Fermi energy, respectively. (a) at V=0. (b) at V=1V. Note that 1V is the flat band voltage indicating voltage losses at the contacts plus ZnO layer of 0.5V.

References

1. Hood SN, Kassal I. Entropy and Disorder Enable Charge Separation in Organic Solar Cells. *J Phys Chem Lett* 2016, **7**(22)**:** 4495-4500.

2. Tessler N, Preezant Y, Rappaport N, Roichman Y. Charge Transport in Disordered Organic Materials and Its Relevance to Thin-Film Devices: A Tutorial Review. *Adv Mater* 2009, **21**(27)**:** 2741-2761.

3. Baranovskii SD. Theoretical description of charge transport in disordered organic semiconductors. *Phys Status Solidi B-Basic Solid State Phys* 2014, **251**(3)**:** 487-525.